International Journal of Multiphase Flow 181 (2024) 105019

Contents lists available at ScienceDirect

International Journal of Multiphase Flow

journal homepage: www.elsevier.com/locate/ijmulflow

Non-negligible buoyancy effect on bubbles travelling in horizontal microchannels of comparable size at small Bond numbers

Jakub A. Cranmer [a,b], Evgenii Sharaborin [c], Sepideh Khodaparast [d], Giovanni Giustini [a], Mirco Magnini [b,*]

[a] Department of Fluids and Environment, The University of Manchester, Manchester, M13 9PL, United Kingdom
[b] Department of Mechanical, Materials and Manufacturing Engineering, University of Nottingham, Nottingham NG7 2RD, United Kingdom
[c] Center for Materials Technologies, Skolkovo Institute of Science and Technology, Moscow, 121205, Russia
[d] School of Mechanical Engineering, University of Leeds, Leeds LS2 9JT, United Kingdom

ARTICLE INFO

Keywords:
Bubbles
Buoyancy
Micro-gravity
Two-phase
Microchannels

ABSTRACT

When a gas bubble is transported by a liquid flow confined within a horizontal channel of comparable size, buoyancy effects are usually assumed to be negligible if the Bond number of the flow is less than unity. However, recent experimental studies showed that buoyancy may still significantly impact the bubble dynamics even when $\mathrm{Bo} \ll 1$, provided that the flow speed is sufficiently small, such that the viscous and inertial forces are weak. To derive a new criterion to assess the significance of buoyancy on the flow of small bubbles in horizontal microchannels, we have performed systematic numerical simulations using the free software Basilisk, covering a wide range of Bond, capillary and Reynolds numbers, $\mathrm{Bo} = 0.004 - 0.4$, $\mathrm{Ca} = 10^{-4} - 0.5$ and $\mathrm{Re} = 0 - 100$, and exploring the bubble-to-channel diameter ratios $d_b/D = 0.2 - 0.9$. We demonstrate that the nondimensional group $\mathrm{Bo}\,(d_b/D)^2/\mathrm{Ca}$ is effective in assessing the importance of buoyancy in flows with negligible inertial effects. When $\mathrm{Bo}\,(d_b/D)^2/\mathrm{Ca} < 0.1$, buoyancy effects are negligible and the bubble travels along the channel axis. When $\mathrm{Bo}\,(d_b/D)^2/\mathrm{Ca} > 10$, buoyancy effects dominate and the bubble travels in the vicinity of the upper wall. For intermediate values, bubbles take equilibrium positions between the channel centre and the wall, and the threshold $\mathrm{Bo}\,(d_b/D)^2/\mathrm{Ca} = 1$ is effective in predicting whether bubbles will travel closer to the channel centre or to the wall. The capillary number at the denominator describes the lift force generated by the deformation of the bubble due to viscous shear, which acts towards the channel centre thus opposing buoyancy. Inertial forces significantly alter the shape and equilibrium position of the bubble when the Weber number of the flow exceeds unity and $\mathrm{Bo}/\mathrm{We} < 1$. Under the action of inertia, bubbles of size comparable to the channel diameter become elongated but remain centred. Smaller bubbles migrate towards the channel wall and do not exhibit a preferential near-wall circumferential position.

1. Introduction

The transport of bubbles by a liquid flow in a microchannel is a classical problem in fluid mechanics and underpins a variety of applications in science and engineering, including, for example, two-phase cooling via microevaporators where bubbles are generated upon boiling (Municchi et al., 2024), membraneless electrolyzers for hydrogen production (Hashemi et al., 2015), micro-chemical reactors (Yang et al., 2014), cell sorting in biomedical and biological applications (Hur et al., 2011; Chen et al., 2014).

When the volume of the bubble is sufficiently small such that its equivalent diameter is smaller than the channel cross-sectional size, see schematic in Fig. 1(a), the bubble takes a spherical or nearly-spherical shape depending on the flow conditions. The shape, speed and lateral position of the bubble depends on the balance of the hydrodynamic forces acting on it. Surface tension and viscous shear are prevailing forces in microchannels, with the former acting to preserve the spherical shape of the bubble and the latter tending to deform it. Inertial forces are often considered of secondary importance owing to the small Reynolds number, however, a number of experimental studies (Di Carlo et al., 2007; Stan et al., 2013) demonstrated that even flows with Reynolds numbers close to unity or below may induce inertial forces that are sufficient to displace the bubble from the channel centreline. Buoyancy is typically neglected for flows in microchannels, due to their small dimensions. A widely accepted criterion to assess the importance of buoyancy on two-phase flows in small channels is based on the Bond

* Corresponding author.
E-mail address: mirco.magnini@nottingham.ac.uk (M. Magnini).

https://doi.org/10.1016/j.ijmultiphaseflow.2024.105019
Received 15 April 2024; Received in revised form 26 July 2024; Accepted 6 October 2024
Available online 10 October 2024

number (Karayiannis and Mahmoud, 2017), which compares buoyancy to surface tension forces, $\mathrm{Bo} = \rho_l g L^2/\sigma$, with ρ_l being the liquid density, g the gravitational acceleration, L a length scale representative of the channel cross-section, and σ the surface tension coefficient. Although other nondimensional groups such as the Eötvös number (Brauner and Moalem Maron, 1992; Ullmann and Brauner, 2007), confinement number (Ong and Thome, 2011; Kew and Cornwell, 1997), capillary length (Triplett et al., 1999), have been used to quantify the importance of buoyancy, these are essentially manipulations of the Bond number and it is often assumed that the effects of buoyancy are negligible on the dynamics of two-phase flows in microchannels when $\mathrm{Bo} < 1$.

However, recent experimental and computational studies of isolated, confined gas bubbles propagating in small channels have revealed that buoyancy may be important even when $\mathrm{Bo} \ll 1$. Atasi et al. (2021) measured the top and bottom thicknesses of the thin lubricating liquid film surrounding long gas bubbles flowing in horizontal circular capillaries, and observed apparent film thickness asymmetries already for $\mathrm{Bo} = \rho_l g D^2/\sigma \approx 0.1$, with D being the channel diameter. Motivated by the work of Atasi et al. (2021), Moran et al. (2021) carried out three-dimensional numerical simulations of slug flow in a horizontal pipe at varying capillary and Bond numbers. They confirmed that, even when $\mathrm{Bo} \ll 1$, the gravity force tends to drain liquid from the top film, thus inducing the previously observed film asymmetry, and reported that the effect of buoyancy was more apparent at small capillary numbers. Magnini et al. (2019) studied the dynamics of long gas bubbles rising in a vertical tube in a cocurrent liquid flow using both experiments and simulations. Buoyancy acted to thicken the liquid film and to increase the bubble rise velocity even in conditions where the Bond number was much smaller than unity. Stan et al. (2011) measured the equilibrium position of nitrogen bubbles suspended in a carrier fluid and flowing in horizontal small channels. When employing a low-viscosity liquid (Dynalene SF) and a rectangular microchannel of height 200 μm, such that $\mathrm{Bo} = 0.01$, bubbles appeared centred within the channel when the capillary number of the flow was $\mathrm{Ca} = \mu_l U_l/\sigma \approx 10^{-2}$, with μ_l and U_l being, respectively, the dynamic viscosity and the average speed of the liquid. However, bubbles progressively lifted off the centre as Ca was reduced and approached the top wall of the channel when $\mathrm{Ca} \approx 10^{-3}$, despite the very small Bond number. On the other hand, when employing a highly viscous silicon oil as a carrier fluid such that $\mathrm{Ca} \approx 10^{-1}$, within a minichannel of height of 2 mm characterised by $\mathrm{Bo} = 1.72$, all bubbles travelled along the channel centre despite $\mathrm{Bo} > 1$. Khodaparast et al. (2015) performed experiments where isolated air bubbles were injected in a horizontal circular microchannel of comparable size ($D = 0.5$ mm) and transported by a laminar liquid flow. The channel was transparent, and the bubbles were visualised from the top using a high-speed camera equipped with a microscope objective, which enabled measurements of bubble shape and speed. A systematic study of the effect of the bubble diameter was conducted, considering both low-viscosity (water) and high-viscosity (glycerol) liquids. The focal plane of the microscope objective was fixed on the centreplane of the tube. As the bubble diameter d_b was reduced to very small values below the pipe diameter, air bubbles transported in glycerol remained in focus and their speed increased monotonically from $U_b/U_l \approx 1$ when $d_b/D \approx 1$ to $U_b/U_l = 2$ when $d_b/D \ll 1$, with U_b being the bubble speed; a plot of the data for bubble speed versus size from Khodaparast et al. (2015) is provided in Fig. 1(b). This suggested that bubbles in glycerol followed the centreline of the pipe without experiencing significant buoyancy effects, which was expected due to the small Bond number, $\mathrm{Bo} = 0.05$. Bubbles transported in water were characterised by a similar value of the Bond number, however, they displayed very different dynamics from the air–glycerol case (see data in Fig. 1(b)). Air-water bubbles appeared lifted off the pipe centreline and their speed decreased as d_b/D was reduced below 1. The drop in speed could be explained by the bubble moving off centre, towards a region where the carrier liquid had a lower velocity. The migration of the bubble towards the top wall was ascribed to buoyancy effects, despite the very small Bond number. As the bubble size was reduced further, below $d_b/D = 0.4$ the bubbles returned to focus and their speed increased towards $U_b/U_l = 2$, as if bubbles were again travelling along the channel centreline with negligible buoyancy effects.

Hence, it is evident that the Bond number alone is insufficient to assess the role of buoyancy on the dynamics of bubbles transported in horizontal channels, because it does not incorporate any description of the forces acting on the bubble and generated from the fluid flow. For bubbles travelling in confined channels, inertial lift and bubble deformation-induced lift are the most relevant hydrodynamic forces acting in the cross-stream direction, and thus together with buoyancy will determine the equilibrium position of the bubble (Di Carlo et al., 2007; Rivero-Rodriguez and Scheid, 2018; Cappello et al., 2023; Stan et al., 2011, 2013). The inertial lift force pushes bubbles away from the centre, whereas the deformation-induced lift pushes bubbles away from the channel wall (Di Carlo et al., 2007; Chan and Leal, 1979; Stan et al., 2011). Analytical and empirical expressions to quantify these forces exist (Zhang et al., 2016; Stan et al., 2013), with inertia calculated proportional to the Reynolds number and the deformation force proportional to the capillary number, however, the validity of these relationships is usually limited to small displacements from the pipe axis and small bubble size. Nonetheless, these models suggest that a more suitable criterion to assess the impact of buoyancy on bubbles travelling in horizontal microchannels should account for some combination of Bond, Reynolds and capillary numbers, to incorporate the effect of hydrodynamic forces that may either counteract (deformation-induced lift) or exacerbate (inertial lift) the gravitational force that tends to attract the bubble towards the top channel wall. To the best of the authors' knowledge, such a criterion is not yet available in the literature.

In this work, we propose a new criterion to quantify the effect of buoyancy on bubbles travelling within horizontal microchannels, which introduces the effect of the fluid flow in modulating the gravitational force. The criterion is developed and validated versus a computational database obtained by performing systematic numerical simulations for a wide range of bubble diameters, Bond, capillary and Reynolds numbers. The proposed criterion is strikingly simple and relies on the ratio between the Bond and capillary numbers.

The rest of this article is organised as follows: in Section 2 a description of the flow problem is presented; the computational framework utilised for the simulations is described in Section 3; the results of this work are illustrated in Section 4 and conclusions are summarised in the final Section 5.

2. Problem formulation

We consider the steady motion of a gas bubble transported in a horizontal circular microchannel by a laminar liquid flow, as exemplified in the schematic in Fig. 1(a). The gravitational force acts vertically downward, and thus buoyancy tends to elevate the bubble above the channel axis. The bubble equivalent diameter and channel diameter are denoted as d_b and D, respectively. We adopt a Cartesian reference frame centred on the channel axis, where x is aligned with the flow direction and y points upwards. Liquid flows with a Poiseuille velocity profile at an average speed U_l. At steady-state, the bubble translates downstream with its centre of mass identified by coordinates (x_b, y_b) and travels at a speed $U_b = dx_b/dt$. Depending on the competition between the surface tension and the other forces acting on the flow, the bubble may become slightly deformed from the spherical shape. When the bubble travels centred in the channel, $y_b = 0$. When the bubble is off-centre, $|y_b| > 0$. The maximum possible distance between bubble centre and channel axis is $y_{b,max} = (D - d_b)/2$, calculated in the limiting case of a spherical bubble in contact with the channel wall.

The dynamics of the bubble can be fully described by the Bond, capillary and Reynolds numbers, and by the bubble-to-channel diameter ratio, expressed as follows:

$$\mathrm{Bo} = \frac{\rho_l g D^2}{\sigma}, \quad \mathrm{Ca} = \frac{\mu_l U_l}{\sigma}, \quad \mathrm{Re} = \frac{\rho_l U_l D}{\mu_l}, \quad d_b^* = \frac{d_b}{D} \tag{1}$$

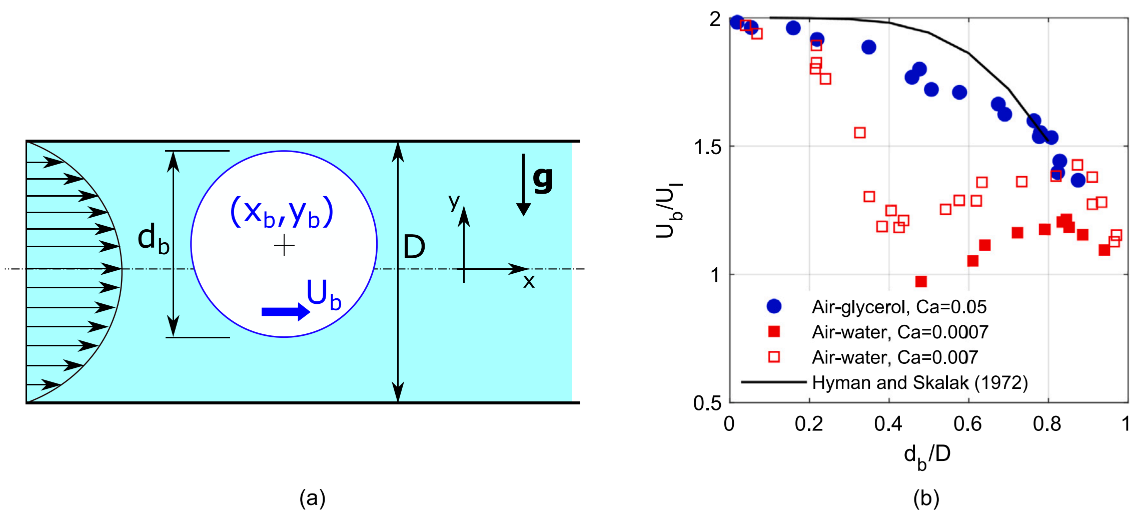

Fig. 1. (a) Schematic of the flow configuration of interest and notation used in this work. A small gas bubble of equivalent diameter d_b ($d_b < D$) propagates at a speed U_b within a horizontal microchannel of diameter D. The bubble is transported by a fully-developed laminar liquid flow of average speed U_l. The coordinates of the centre of mass of the bubble are indicated as (x_b, y_b). The gravitational force is oriented vertically downward. (b) Summary of the experimental data for bubble speed versus size measured within a horizontal circular microchannel of $D = 0.5$ mm by Khodaparast et al. (2015). (For interpretation of the references to colour in this figure legend, the reader is referred to the web version of this article.)

The liquid speed U_l is chosen as a velocity scale for Ca and Re as this is usually an input parameter in experiments and simulations, and thus its value is known beforehand. The liquid-to-gas density and viscosity ratios are assumed to be sufficiently large such that a stress-free condition applies to the surface of the bubble. Since we assume that $\rho_l/\rho_g \gg 1$, with ρ_g being the density of the gas, the Bond number in Eq. (1) is evaluated based on the liquid density.

In the experiments of Khodaparast et al. (2015) in a $D = 0.5$ mm channel, the air–glycerol flow was characterised by Bo = 0.0514 and the data plotted in Fig. 1(b) refer to Ca = 0.05. The Reynolds number was very small, Re $\approx 10^{-3}$, owing to the high viscosity of glycerol. The bubbles appeared in focus on the camera images over the range of d_b/D studied, suggesting a centred position. Their speed was in good agreement with the analytical solution for the axisymmetric creeping flow of spherical bubbles obtained by Hyman and Skalak (1972), represented with a black solid line in Fig. 1(b). The experimental data remained up to 10% below the predictions in the range $d_b/D = 0.2 - 0.7$, which was attributed to some small, but not negligible, buoyancy effects, which could have slightly displaced the bubbles off-centre. Air-water bubbles were characterised by a Bond number of Bo = 0.036, much smaller capillary numbers and Reynolds numbers Re > 1. Fig. 1(b) includes the data for Ca = 0.0007 (Re = 34) and Ca = 0.007 (Re = 340). In both cases, the bubble was observed to be elevated from the channel centre and its speed decreased monotonically upon reducing the bubble size from $d_b/D = 1$ to $d_b/D = 0.5$. Besides buoyancy, the effect of inertial lift cannot in principle be ruled out in the air–water configuration. However, inertial lift tends to push the bubble away from the channel centre, and thus the bubble speed for Ca = 0.007 would be expected to be smaller than that for Ca = 0.0007, contrary to the experimental data.

An estimate of the magnitude of buoyancy, inertial lift and deformation-induced lift for the flow configurations discussed above can be computed using available correlations. The buoyancy force acting on the bubble can be readily calculated as:

$$F_g = \rho_l \frac{4}{3}\pi r_b^3\, g \tag{2}$$

with $r_b = d_b/2$ being the bubble radius. The buoyancy force is always directed towards the top wall in a horizontal channel. For bubbles of size comparable to that of the channel, the bubble deformation-induced lift force is always directed towards the channel axis and can be estimated using the model originally proposed by Chan and Leal (1979), later rewritten by Stan et al. (2011) as:

$$F_d = 2\mu_l U_l r_b \mathrm{Ca} \left(\frac{r_b}{D}\right)^3 \frac{y_b}{D} f(\lambda) \tag{3}$$

where $f(\lambda)$ is a function of the viscosity ratio between gas and liquid and $f(\lambda \approx 0) = 919$ (Chan and Leal, 1979). However, Stan et al. (2013) measured the equilibrium positions of drops and bubbles transported in horizontal microchannels and suggested that Eq. (3) underpredicted the lift force by a factor proportional to Ca. By fitting their experimental data for bubbles transported at very small Reynolds numbers (Re < 0.01), they proposed the following correlation to calculate the deformation-induced lift:

$$F_d = C_L \mu_l U_l r_b \left(\frac{r_b}{D}\right)^3 \frac{y_b}{D} \tag{4}$$

where $C_L = 100 - 300$ depending on the carrier liquid; here, the value $C_L = 315$ corresponding to nitrogen bubbles carried in Dynalene SF liquid will be used. Note that both Eqs. (3) and (4) require knowledge of the distance y_b between the bubble and the tube centre. Eq. (4) is applicable to nearly-spherical bubbles travelling near the channel centre, $y_b/D \leq 0.15$, small capillary and Reynolds numbers, Ca < 0.01 and Re < 0.01. The inertial lift force acting on the bubble can be estimated using an empirical correlation derived by Stan et al. (2011) based on an empirical fit of the experimental data of Di Carlo et al. (2009):

$$F_i = 10\mu_l U_l r_b \mathrm{Re} \left(\frac{r_b}{D}\right)^2 \frac{y_b}{D} \tag{5}$$

Eq. (5) was derived by fitting data for spherical polystyrene particles transported in water and travelling near the channel centre ($y_b/D \leq 0.1$); the resulting force pushed the particles away from the channel axis.

Plots of the hydrodynamic forces calculated using Eqs. (2)–(5) at varying bubble size are presented in Fig. 2 for (a) air–glycerol and (b,c) air–water under the conditions studied by Khodaparast et al. (2015). Since the vertical elevation of the bubble from the channel centre y_b is not known, the term y_b/D in the expressions for deformation and inertial lift forces is set to $y_b/D = 0.1$, which yields the highest lift force possible within the limit of validity of the correlations. The magnitudes of buoyancy and deformation-induced lift are comparable in the case of glycerol, Fig. 2(a), thus suggesting that the bubble may reach an equilibrium position in the proximity of the centre of the channel, in agreement with the experiment. Buoyancy is significantly larger than the other forces in the case of air–water at Ca = 0.0007, Fig. 2(b). This may explain the decreasing trend in bubble speed when decreasing d_b/D observed in Fig. 1(b). However, the magnitude of the inertial and deformation lift forces is likely to be underestimated if the bubble

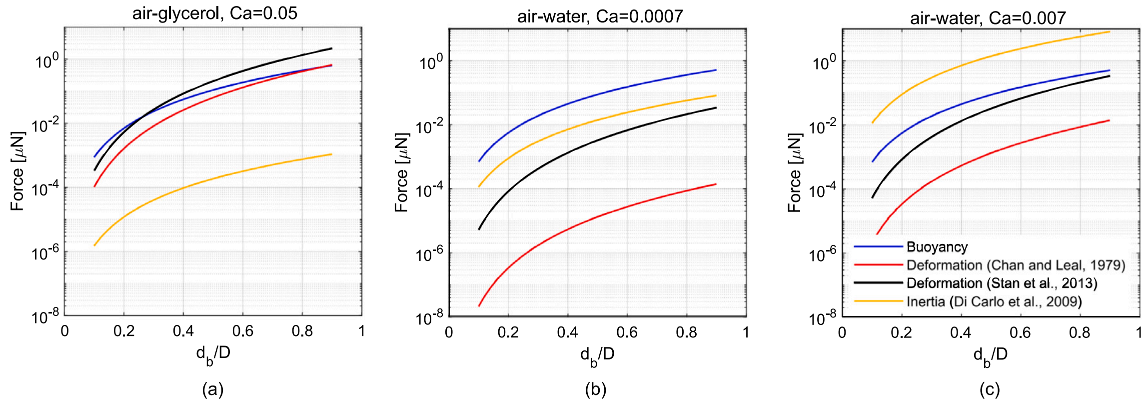

Fig. 2. Estimation of the lateral migration forces acting on the air bubbles transported by (a) glycerol and (b,c) water in the experiments of Khodaparast et al. (2015). The legend in (c) applies also to (a) and (b). The buoyancy force is calculated using Eq. (2); the deformation-induced lift force is calculated using both Eq. (3) derived by Chan and Leal (1979) anf Eq. (4) from Stan et al. (2013); the inertial lift force is calculated using Eq. (5) proposed by Di Carlo et al. (2009). (For interpretation of the references to colour in this figure legend, the reader is referred to the web version of this article.)

migrates further than $y_b/D = 0.1$ from the channel centre, as Stan et al. (2013) observed that the overall lift force increased more than linearly with y_b/D when $y_b/D > 0.15$. At higher Reynolds numbers, Fig. 2(c), the calculated inertial lift force becomes dominant, and thus the bubble would be expected to further migrate away from the channel axis. However, the bubbles in the experiment travelled faster, see Fig. 1(b), and for $d_b/D \leq 0.2$ their high speed may suggest that bubbles were centred.

In summary, the available correlations to calculate the hydrodynamic lift forces experienced by the bubble are limited in applicability and do not give a satisfactory quantitative prediction of the forces opposing buoyancy. Nonetheless, the nondimensional groups emerging from the ratio of each pair of forces reveal valuable insights. The ratio of buoyancy over deformation lift force resulting from Eqs. (2) and (4) suggests that $F_g/F_d \propto \mathrm{Bo}/\mathrm{Ca}$. It will be shown in Section 4.1 that a nondimensional group derived from the ratio of Bond and capillary numbers is effective in assessing buoyancy effects in flows with negligible inertia. The ratio of buoyancy over inertial lift force resulting from Eqs. (2) and (5) suggests that $F_g/F_i \propto \mathrm{Bo}/(\mathrm{Ca}\,\mathrm{Re})$, or Bo/We with $\mathrm{We} = \mathrm{Ca}\,\mathrm{Re}$ being the Weber number, and it will be shown in Section 4.2 that this group is effective in predicting the threshold above which inertial forces become relevant.

3. Computational framework

3.1. Basilisk flow solver

Direct numerical simulations of the flow configuration illustrated in Fig. 1(a) were performed using Basilisk flow solver (basilisk.fr). The simulation setup utilised in this work was adapted from that documented in Sharaborin et al. (2021a), who utilised Basilisk to study the dynamics of elongated bubbles flowing in a microchannel and validated the solver against experimental data from the literature. The unsteady, incompressible Navier–Stokes equations for a Newtonian fluid are solved by employing a Volume Of Fluid (VOF) method to track the interface between the immiscible liquid and gas phases. Basilisk solves the continuity, momentum and volume fraction equations formulated as follows:

$$\nabla \cdot \boldsymbol{u} = 0 \tag{6}$$

$$\rho\left(\frac{\partial \boldsymbol{u}}{\partial t} + \boldsymbol{u}\cdot\nabla\boldsymbol{u}\right) = -\nabla p + \nabla\cdot\left[\mu(\nabla\boldsymbol{u} + \nabla^T\boldsymbol{u})\right] + \rho\boldsymbol{g} + \sigma\kappa\boldsymbol{n}\delta_s \tag{7}$$

$$\frac{\partial f}{\partial t} + \boldsymbol{u}\cdot\nabla f = 0 \tag{8}$$

where $\boldsymbol{u}$ denotes the fluid velocity, t the time, p the pressure, f the liquid volume fraction, $\boldsymbol{g}$ the gravitational force vector, κ the interface curvature, $\boldsymbol{n}$ the interface normal vector, and δ_s is a delta function that ensures that the surface tension force is active only on interfacial cells. The single-fluid density and viscosity are calculated as averages of liquid and gas properties, weighted by the local volume fraction value.

Basilisk adopts second-order accurate discretisation methods in both space and time (Popinet, 2015). The temporal integration of the convective term of the momentum equation is performed using a Bell–Colella–Glaz advection unsplit upwind scheme (Bell et al., 1989), whereas the viscous term is computed implicitly. The surface tension force is implemented using a balanced-force algorithm (Popinet, 2009) and the interface topology, namely curvature and normal vector, is reconstructed using a second-order height function algorithm. The volume fraction advection equation is discretised using a geometric VOF method based on a dimension-splitting PLIC (Piecewise Linear Interface Calculation) algorithm (Youngs, 1982). The time-step of the simulations is adaptive and set by a maximum Courant–Friedrichs–Lewy (CFL) number of 0.5. Basilisk adopts an adaptive quad/octree spatial discretisation of the flow equations that enables a powerful adaptive mesh refinement, which will be crucial in the present case to accurately resolve the interface dynamics in a computationally efficient manner.

3.2. Geometry, boundary conditions and mesh

The systematic analysis of the influence of Bond, capillary, and Reynolds numbers on the flow of bubbles of different diameters required about 400 simulations. Therefore, simulations were performed by adopting a two-dimensional planar flow configuration in order to finely investigate the parameter space. The flow configuration coincides with that depicted in Fig. 1(a). Two-dimensional simulations for an analogous flow problem were also adopted by Stan et al. (2011) and Mortazavi and Tryggvason (2000), who observed small differences in the equilibrium positions of bubbles (Stan et al., 2011) and droplets (Mortazavi and Tryggvason, 2000) compared to three-dimensional simulations. Two- and three-dimensional simulations for a few selected cases were also performed in the present work and the comparison is illustrated in Appendix. These verified that the steady-state positions of the bubbles, which are our main parameters of interest, are in good agreement, thus supporting the choice of using computationally cheaper two-dimensional simulations.

All quantities in the simulation setup were rescaled by the channel diameter set as $D = 1$, by the average liquid velocity set as $U_l = 1$, and by the liquid density set as $\rho_l = 1$. The length of the channel was varied between $L = 20D$ and $80D$, as necessary to achieve steady bubble dynamics. A fully-developed parabolic velocity profile was set at the channel inlet, with a maximum velocity of $1.5U_l$ at the centre owing to the two-dimensional geometry, while a zero gradient condition was set

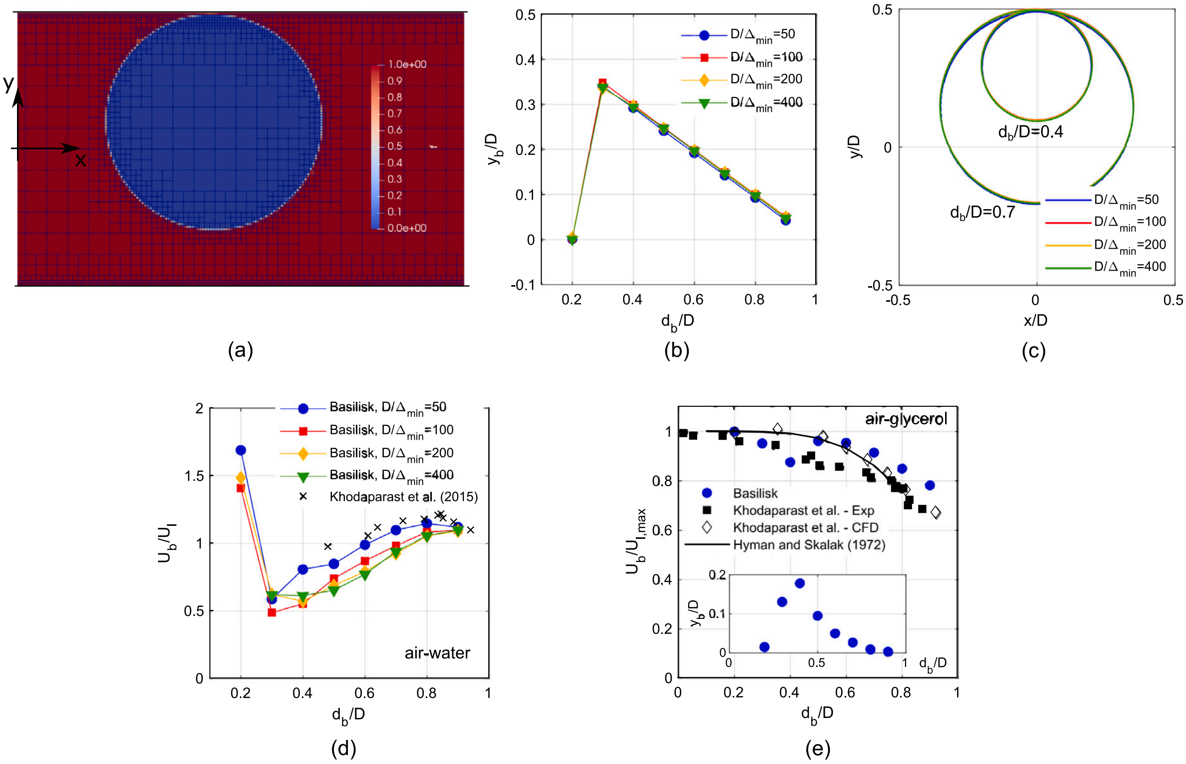

Fig. 3. (a) Computational mesh used to perform the simulations presented in this work, here displayed for a case run with $d_b/D = 0.8$; the colour map shows the liquid volume fraction field. The smallest cell size is $\Delta_{min}/D = 0.01$, the largest cell size is $\Delta_{max}/D = 0.08$. (b,c,d) Bubble elevation, shapes and speed for different meshes at conditions matching the experiments of Khodaparast et al. (2015) for air bubbles transported in water at Ca = 0.0007; in (d), bubble velocities from simulations are compared with the experimental data. (e) Comparison of Basilisk simulation results with benchmark data from Khodaparast et al. (2015) for air–glycerol at Ca = 0.05. In (b,c,d), Δ_{min} refers to the mesh size at the maximum level of refinement. The inset in (e) plots the bubble elevation extracted from the Basilisk simulations. (For interpretation of the references to colour in this figure legend, the reader is referred to the web version of this article.)

for the pressure. At the channel walls, a no-slip and fully hydrophilic boundary condition was applied by adopting a Brinkman penalisation method as described by Sharaborin et al. (2021b,a). At the outlet, a zero gradient condition applies for the velocity, and the pressure is set to a constant reference value. As an initial condition for the simulation, a circular bubble of diameter d_b is patched at the centre of the channel ($y_b = 0$), near the inlet section. From this initial configuration, the simulation evolves in time until steady-state values of the bubble velocity and position of the centre of mass are achieved.

The liquid viscosity, surface tension and gravitational acceleration are set for each simulation run according to the input values of Bo, Ca and Re, with $\mu_l = 1/\mathrm{Re}$, $\sigma = 1/(\mathrm{Ca\,Re})$, and $g = -\mathrm{Bo}/(\mathrm{Ca\,Re})$. The liquid-to-gas density and viscosity ratios are fixed to 1000 and 100, respectively. The range of values of the nondimensional groups indicated in Eq. (1) investigated in this work is as follows: Bo = 0.004 – 0.4, Ca = 0.0001 – 0.5, Re = 0 – 100, $d^* = d_b/D = 0.2$ – 0.9. Lower values of the Bond number are unnecessary because, as it will be shown, below a certain value of Bo/Ca the bubble dynamics become independent of Bo. Likewise, higher values of Bo are not considered because the bubble dynamics remain unchanged above a certain threshold on Bo/Ca.

The computational mesh makes use of Basilisk's very efficient quad/octree adaptive mesh refinement. Fig. 3(a) shows an example of the mesh used in this work. For an indicative channel length of $20D$, the maximum cell size is set to level 8, which yields square cells of size $\Delta_{max}/D = 0.08$ where the mesh is not refined. The maximum level of refinement is set to 11, which yields a smallest cell size of $\Delta_{min}/D = 0.01$ (100 cells within a channel diameter) achieved at the gas–liquid interface, near the channel walls, and in the presence of strong velocity gradients. A mesh convergence analysis was performed at conditions emulating the air–water experiments at Ca = 0.0007 of Khodaparast et al. (2015). Four different meshes were employed by varying the maximum level of refinement from level 10 ($D/\Delta_{min} = 50$) to level 13 ($D/\Delta_{min} = 400$). The results are reported in Fig. 3(b,c,d), which plot the vertical elevation of the bubbles above the centreline, the profiles of the bubbles for two selected bubble diameters ($d_b/D = 0.4$ and 0.7), and the bubble speed; all data were extracted when the bubble dynamics had reached steady-state conditions. Fig. 3(b,c) indicate that all meshes lead to the same results in terms of bubble terminal position and shapes, with data points and bubble profiles overlapping almost perfectly. In particular, the differences in the steady-state values of the bubble elevation y_b remain below 2% among all meshes tested. The bubble velocities displayed in Fig. 3(d) exhibit some apparent differences between levels 10 and 11, with an average difference of 13% calculated across all the d_b tested. This reduces to 7% and 2% when comparing level 11 with 12, and 12 with 13, respectively. It is interesting to note that the differences in the bubbles speeds obtained with the four meshes do not result in appreciable differences in the corresponding bubbles shapes and positions. Therefore, since in this work we are primarily interested in the terminal positions of the bubbles, the mesh with $D/\Delta_{min} = 100$ was utilised to perform all the simulations presented in this article, as it provided the best compromise between accuracy of the results and computational cost of the simulations. Additional tests performed with finer meshes in the unrefined regions of the channel did not yield appreciable differences.

3.3. Validation

The numerical model was first validated against two air–water and air–glycerol test configurations from Khodaparast et al. (2015). The comparison of the bubble speed at varying d_b is displayed in Fig. 3(d) for air–water and Fig. 3(e) for air–glycerol. The numerical simulations follow quite well the experimental trends, with some minor differences

Table 1
Validation against experiments and two-dimensional planar simulations performed by Stan et al. (2011). Their data are taken from Table 1 in the Appendix of their paper. Low capillary number experiments were performed with fluid Dynalene SF as carrier within a horizontal rectangular microchannel of height of 200 μm and width 125 μm. High capillary number experiments were performed with silicone oil RT500 as carrier fluid within a horizontal rectangular minichannel of height of 2 mm and width 1.17 mm. The bubbles cross-stream positions y_b were measured from high-speed camera images taken from the side of the transparent PDMS channels.

Case	Fluid (liquid/gas)	Ca	Re	Bo	d_b/D	y_b/D Measured (Stan et al., 2011)	y_b/D Simulated (Stan et al., 2011)	y_b/D Basilisk
1	DySF/nitrogen	0.0039	0.0074	0.0116	0.46	0.22	0.23	0.26
2	DySF/nitrogen	0.004	0.0074	0.0116	0.6	0.13	0.17	0.19
3	DySF/nitrogen	0.007	0.013	0.0116	0.5	0.08	0.18	0.2
4	DySF/nitrogen	0.0122	0.022	0.0116	0.5	0.02	0.17	0.12
5	RT500/nitrogen	0.23	0.037	1.72	0.48	0.13	0.16	0.13
6	RT500/nitrogen	0.42	0.07	1.72	0.36	0.09	0.14	0.11
7	RT500/nitrogen	0.55	0.095	1.72	0.4	0.04	0.11	0.06
8	RT500/nitrogen	0.75	0.12	1.72	0.44	0.02	0.06	0.03

due to the two-dimensional geometry adopted. The average deviation between experimental and numerical U_b/U_l for air–water when using the level 11 mesh is 12%. The underprediction of the bubble speed in the simulation can be ascribed to the planar Poiseuille velocity profile having a smaller maximum value than in the axisymmetric case. Since the bubbles in glycerol travel near the centre, the bubble speed data in Fig. 3(e) are rescaled by the maximum liquid speed at the channel axis so that both axisymmetric and planar solutions converge to $U_{l,max}$ as $d_b \to 0$. As explained in Section 2, the experimentally measured values of U_b remained below the theoretical solution for creeping axisymmetric flow of Hyman and Skalak (1972), whose predictions coincided with the results of axisymmetric CFD simulations performed by Khodaparast et al. (2015). The authors ascribed this to some residual buoyancy effects, that might have also induced errors in the calculation of the bubble size from the high-speed video images. Our two-dimensional planar simulations confirm the presence of weak buoyancy effects, see the inset in Fig. 3(e) where the bubble elevation data are presented, with the maximum distance from the centre $y_b/D = 0.18$ being achieved for $d_b/D = 0.4$. This corresponds to a slight dip in U_b. The average deviation in $U_b/U_{l,max}$ between simulations and experiments for air–glycerol is 6%, which can be considered satisfactory. Note that the largest deviations, about 10%, occur for $d_b/D > 0.6$, because the bubble speed rescaled by $U_{l,max}$ converges to different values as $d_b \to D$ depending on the channel geometry, i.e. $U_b/U_{l,max} \approx 0.5$ ($U_b/U_l \approx 1$) in the axisymmetric case and $U_b/U_{l,max} \approx 0.67$ ($U_b/U_l \approx 1$) in the planar geometry.

Additional validation tests were performed by comparing simulation results with the experiments of Stan et al. (2011), who measured the equilibrium positions of nitrogen bubbles transported by low- and high-viscosity liquids within horizontal rectangular channels, spanning the range $\mathrm{Ca} = 10^{-3} - 1$ and $\mathrm{Bo} = 10^{-2} - 1$, with $\mathrm{Re} \ll 1$. Eight experimental conditions were tested, the details of which are listed in Table 1. Stan et al. (2011) performed two-dimensional planar simulations for the same eight cases using a Level Set method, whose results are also included in Table 1; the authors also verified for a few selected cases that two-dimensional and three-dimensional simulations yielded the same transverse positions of the bubbles. The equilibrium positions of the bubbles obtained with Basilisk are in excellent agreement with the experiments except for cases 3 and 4. However, for these two cases our simulations agree well with the numerical results of Stan et al. (2011), thus suggesting some potential issues with the experimentally measured values. The flow focussing device utilised in the experiment produced closely spaced trains of bubbles, and the distance between consecutive bubbles decreases upon an increase of the liquid flow rate (Garstecki et al., 2004). Therefore, it is plausible that the vicinity of the bubbles impacted their equilibrium positions for cases 3 and 4.

4. Results

4.1. Flows with negligible inertial effects

In this section, the results of simulations obtained for negligible inertial effects ($\mathrm{Re} = 0$) are presented. The simulations were run in a Stokes flow regime, neglecting the convective term in the momentum Eq. (7). In the absence of inertia, the only forces acting on the bubble in the cross-stream direction are buoyancy and the deformation-induced lift.

4.1.1. Bubble dynamics at varying capillary number

A first set of simulations was run by setting the Bond number to $\mathrm{Bo} = 0.04$, that is, similar to the conditions experimentally studied by Khodaparast et al. (2015), and varying the capillary number from $\mathrm{Ca} = 0.001$ to 0.1. The temporal evolution of the vertical position of the centre of mass and of the speed of the bubble, from the beginning of the simulation until steady-state conditions, is shown in Fig. 4(a) and (b) for $\mathrm{Ca} = 0.01$; note that both y_b and U_b are plotted as a function of the axial coordinate of the centre of mass of the bubble, x_b. Bubbles attain steady positions after travelling less than 10 channel diameters. The duration of the transient regime increases with decreasing the bubble size, because under these conditions smaller bubbles migrate further away from their initial position $y_b = 0$ at $t = 0$. On the other hand, the transient regime is very short for $d_b/D = 0.2$ as the bubble remains close to the pipe axis and thus quickly attains steady-state conditions.

The bubble elevation and speed at steady-state for all capillary numbers tested are reported in Fig. 4(c,d). For $\mathrm{Ca} \le 0.005$, bubble elevations and speeds for corresponding bubble diameters coincide and thus the results are independent of the capillary number. Under these conditions, the bubbles travel above the channel centreline in the proximity of the top wall. As the bubble diameter is reduced, the bubble speed decreases monotonically since the bubbles move further away from the channel centre where the velocity of the carrier liquid is the fastest. A change in trend is apparent when $d_b = 0.2D$ and the bubbles remain centred. This can be explained by buoyancy having a reduced effect for very small bubbles, as the net buoyancy force scales with the bubble volume. A similar trend was observed by Khodaparast et al. (2015) for air–water bubbles of small size, $d_b/D < 0.4$ see Fig. 1(b). When $\mathrm{Ca} > 0.005$, bubbles depart from the top wall and travel closer to the pipe axis as the capillary number, and thus the viscous force, is increased. Hence, their speed increases as they are carried by faster fluid. This suggests that viscous forces are able to generate a net lift force that counteracts buoyancy as the capillary number increases. It is interesting to observe that the nonmonotonic trend of y_b/D versus d_b/D is maintained as $d_b/D \to 0$ for increasing capillary numbers, e.g. for $\mathrm{Ca} = 0.05$, which was also observed by Stan et al. (2011) for nitrogen bubbles of size $d_b/D < 0.5$ travelling in liquid hydrocarbon in a horizontal microchannel at smaller capillary number, $\mathrm{Ca} = 0.0038$, but similar $\mathrm{Bo}/\mathrm{Ca} = 0.79$. Bubbles become approximately centred for $\mathrm{Ca} = 0.1$, with $y_b/D < 0.05$ and the bubble speed following quite well a monotonically increasing trend with $d_b \to 0$ in agreement with Hyman and Skalak (1972) theory.

In order to understand the origin of the lift force that pushes bubbles towards the pipe axis as the capillary number of the flow is increased, Fig. 5 displays the bubble shapes, streamlines and pressure profiles around the bubbles for three selected cases at increasing capillary

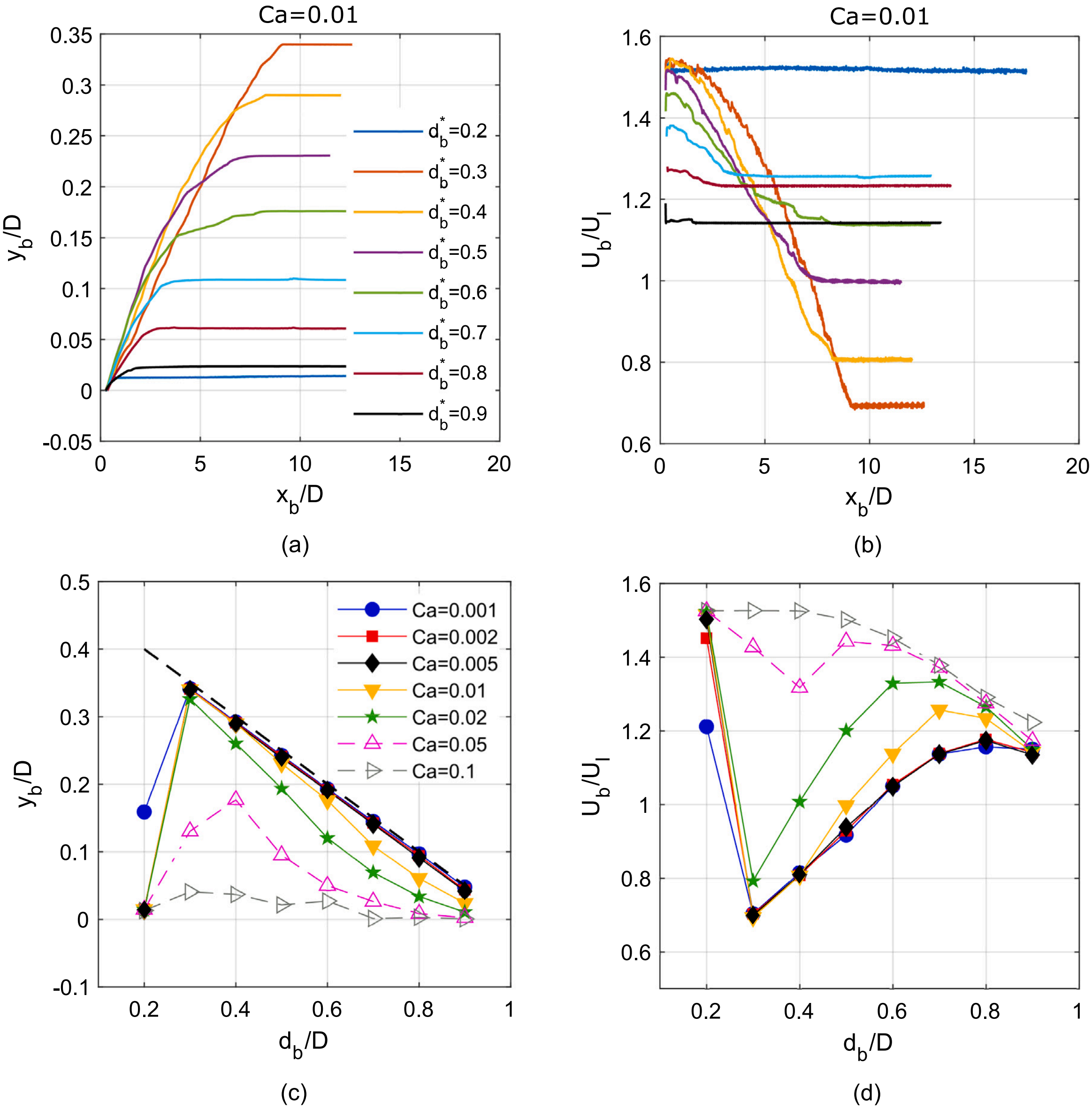

Fig. 4. Summary of all simulation results for $\mathrm{Bo} = 0.04$. (a,b) Temporal evolution of the (a) vertical position of the centre of mass of the bubble and (b) bubble speed for $\mathrm{Ca} = 0.01$; d_b^* indicates the nondimensional equivalent bubble diameter, $d_b^* = d_b/D$. (c,d) Plots of the (c) vertical position of the centre of mass of the bubble and (d) bubble speed at varying bubble size and capillary number. The black dashed line in (c) identifies the maximum elevation possible within the channel for the centre of mass of a spherical bubble, $y_{b,max} = (D - d_b)/2$. In (c,d), full symbols and solid lines are used for datapoints with $\mathrm{Bo}/\mathrm{Ca} > 1$, whereas empty symbols and dashed lines are used for datapoints with $\mathrm{Bo}/\mathrm{Ca} < 1$. (For interpretation of the references to colour in this figure legend, the reader is referred to the web version of this article.)

numbers and constant bubble size. Streamlines in Fig. 5(a,b,c) are calculated from a reference frame moving with the bubble and thus represent the flow field $\boldsymbol{u} - U_b\hat{\boldsymbol{i}}$, with $\hat{\boldsymbol{i}}$ being the unit vector in the x direction. The pressure profiles plotted in Fig. 5(d) are extracted over a circle enclosing the bubble, depicted in Fig. 5(a,b,c) and coloured according to the local pressure values; pressure is displayed at the net of the hydrostatic head, $p' = p - \rho_l g(R - y)$, and is rescaled by a reference pressure $p_{ref} = \mu_l U_l/D$. The zero pressure reference is located at $\theta = 0$, with θ measured as indicated in Fig. 5(a). The results for $\mathrm{Bo} = 0.04$ and capillary numbers of $\mathrm{Ca} = 0.005, 0.01$ and 0.02 presented in Fig. 5 correspond to configurations where the bubble ($d_b/D = 0.5$) gradually detaches from the top wall as the capillary number increases. The streamlines and pressure profiles exhibit common features in these three cases. On a reference frame translating steadily downstream at the bubble speed U_b, the fluid near the walls travels backward at a speed $-U_b$, whereas the fluid near the channel centreline travels forward at a speed $1.5U_l - U_b$. Hence, four recirculation regions are formed, with two counterclockwise rotating vortices established on the channel top-half which interact with the bubble and impact the pressure field around it. Pressure is positive around the bubble in the first and third quadrants, where the streamlines impact the bubble surface, and is negative in the second and fourth quadrants, where the streamlines leave the bubble. The pressure profile exhibits two local maxima in the first ($\theta = 65°{-}75°$) and third ($\theta = 200°{-}220°$) quadrants, in the correspondence of two stagnation points on the surface of the bubble. Since the relative velocity between bubble and fluid is higher near the wall, the overpressure generated in the first quadrant is higher than that in the third quadrant. Two pressure minima are also established in the second ($\theta = 100°{-}115°$) and fourth ($\theta \approx 330°$) quadrants, in the vicinity of two other stagnation points on the bubble surface. The pressure minima on the second quadrant is lower than that on the fourth quadrant, owing to the higher relative speed between fluid and bubble. The overall result of the integral of the pressure profile around the bubble (i.e., the integral of $p\sin(\theta)$) is a downward oriented

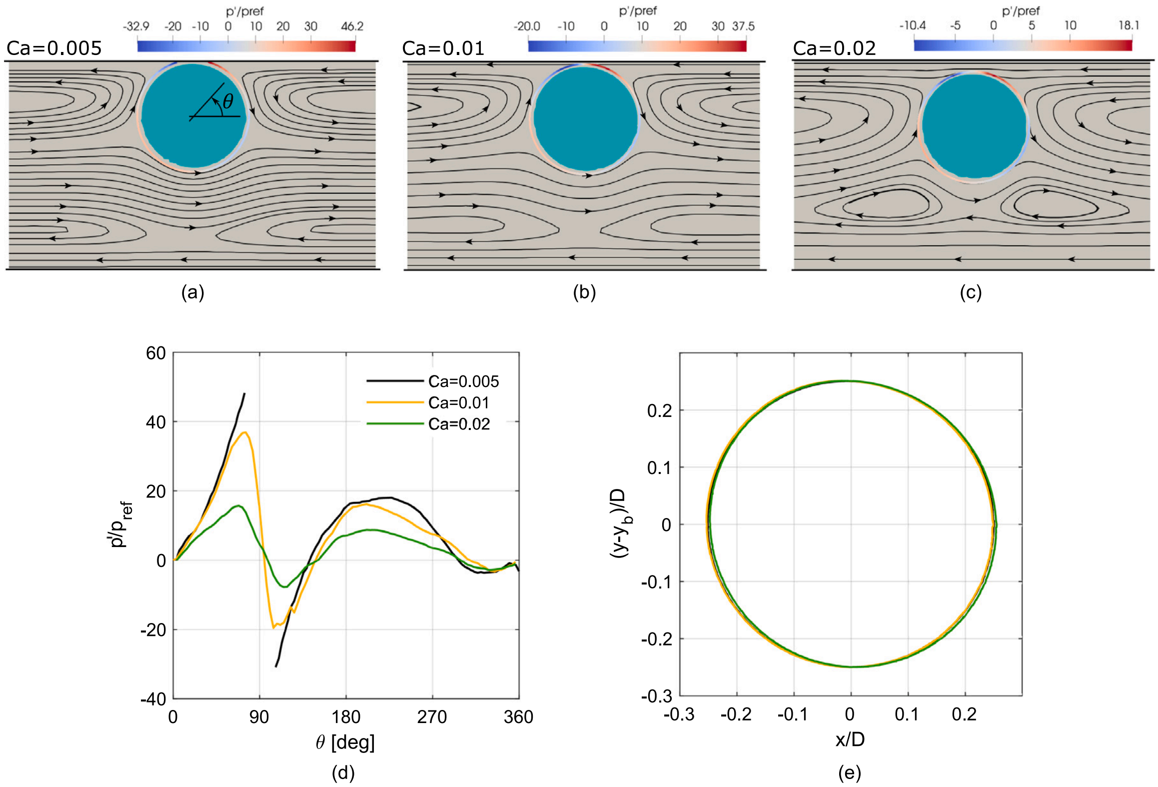

Fig. 5. (a,b,c) Bubble shape, streamlines and circumferential pressure distributions around the bubble for Bo = 0.04, $d_b/D = 0.5$ and three selected capillary numbers; streamlines are shown in a reference frame moving with the bubble; pressure values are reported at the net of the hydrostatic head, $p' = p - \rho_l g(R - y)$, and are rescaled with a pressure reference calculated as $p_{ref} = \mu_l U_l / D$. (d) Circumferential pressure profiles extracted on the circles around the bubbles depicted in (a,b,c), and (e) bubble shapes. The legend in (d) applies also to (e). The pressure profile in (d) for Ca = 0.005 is incomplete as the circle used for its calculation extends outside the simulation domain. The bubble shapes in (e) are vertically translated in order for the bubble centres to coincide . (For interpretation of the references to colour in this figure legend, the reader is referred to the web version of this article.)

force that, at equilibrium, balances the upward oriented buoyancy force acting on the bubble and supports the formation of a thin liquid film separating the bubble from the top wall. A similar pressure pattern was observed by Feng et al. (1994) around rigid spherical particles moving near the wall in a planar Poiseuille flow and by Rivero-Rodriguez and Scheid (2018) for deformable bubbles transported by a three-dimensional Poiseuille flow. In the case of deformable objects such as bubbles, the nonuniform pressure profile deforms the bubble by locally decreasing its curvature on the first and third quadrants, and increasing it on the second and fourth quadrants, as can be observed in Fig. 5(e) where the bubble profiles are depicted. The asymmetric velocity profile around the bubble due to the presence of the wall and the bubble deformation contribute to the generation of the lift force pushing the bubble away from the wall, typically referred to as deformation-induced lift force (Magnaudet et al., 2003). Under the assumption of small capillary and Reynolds numbers, small bubble deformation and bubbles sufficiently far from the channel wall, Chan and Leal (1979) used a matched asymptotic expansion method to derive the analytical expression reported in Eq. (3) to estimate the lift force induced by bubble deformation, but disregarding the effect of the channel walls, for bubbles travelling in a Poiseuille flow within a channel. Eq. (3) suggests that the lift force increases linearly with the capillary number (and thus viscous shear) and with the distance of the bubble from the channel axis. Inspection of the bubble positions in Fig. 5(a–c) reveals that the equilibrium position of the bubble moves farther from the wall as the capillary number is increased. Since Bond number and bubble size are the same in the three cases, the buoyancy force has the same magnitude and thus at equilibrium the lift force must be the same in all cases. In order for the lift force to be the same, the increase in the capillary number in Eq. (3) must be balanced by a decrease of y_b/D, which is achieved by the bubble moving closer to the channel centre. Note that the application of Eq. (3) is only qualitative in the conditions simulated, because the capillary number and distance from the wall are well outside the range of validity of Chan and Leal (1979) theory. It is likely that the lift force increases more than linearly with y_b/D as the bubble approaches the channel wall, as demonstrated in the experiments of Stan et al. (2013) when $y_b/D > 0.15$.

Bubble shapes corresponding to selected capillary numbers from the conditions investigated in this section are provided in Fig. 6. Bubbles appear almost perfectly circular for Ca = 0.002, see Fig. 6(a). At such a low capillary number, viscous effects are weak and not sufficient to generate a lift force able to counteract gravity, and hence the bubbles travel along the top wall. As Ca $\geq$ 0.02, Fig. 6(b–d), the equilibrium position of the bubbles progressively migrates away from the top wall and bubbles deform to a larger extent as Ca is increased, becoming slightly elongated in the flow direction. This deformation is the result of the increasingly dominant viscous effects which are responsible for the force that takes bubbles away from the wall. In summary, the change in trend from a near-wall to a centred equilibrium position for the bubbles occurs gradually between Ca = 0.01 and Ca = 0.1. Interestingly, this corresponds to the range Bo/Ca = 4 – 0.4, supporting the initial hypothesis that Bo/Ca $\approx$ 1 may be an effective threshold in assessing the impact of buoyancy. This will be further verified in the next section upon systematic variation of the Bond number.

Last, the simulation results in terms of terminal vertical position of the bubble centre at varying bubble size for different capillary numbers are compared to the predictions offered by the theory of Chan and Leal (1979) and the empirical correlation of Stan et al. (2013) which, up to the Authors' knowledge, are the only available methods to estimate the deformation-induced lift force for bubbles transported in Poiseuille

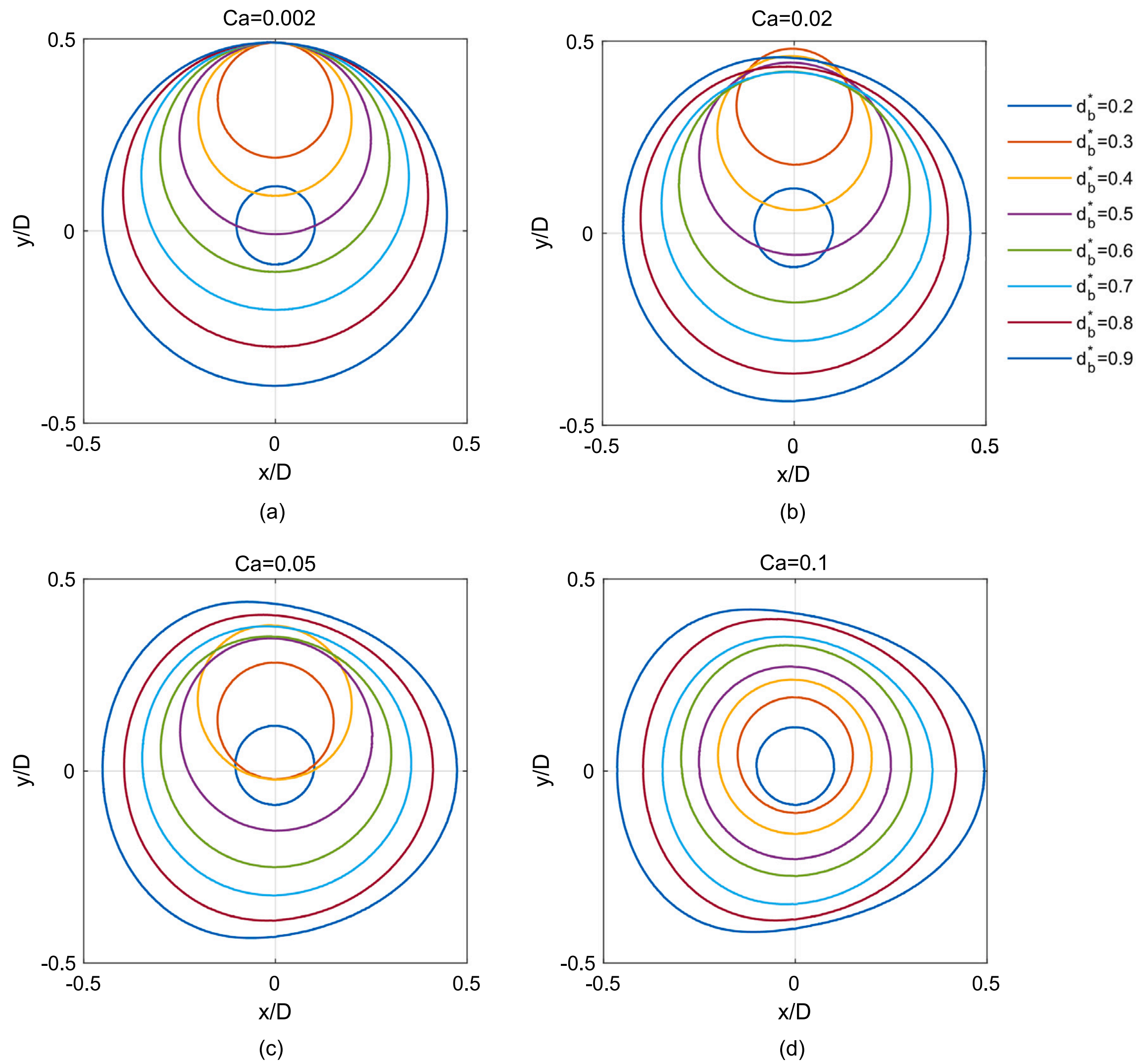

Fig. 6. Bubble shapes for selected capillary numbers at Bo = 0.04. The x coordinates of the interface points of each bubble are shifted to match the corresponding value of x_b. (For interpretation of the references to colour in this figure legend, the reader is referred to the web version of this article.)

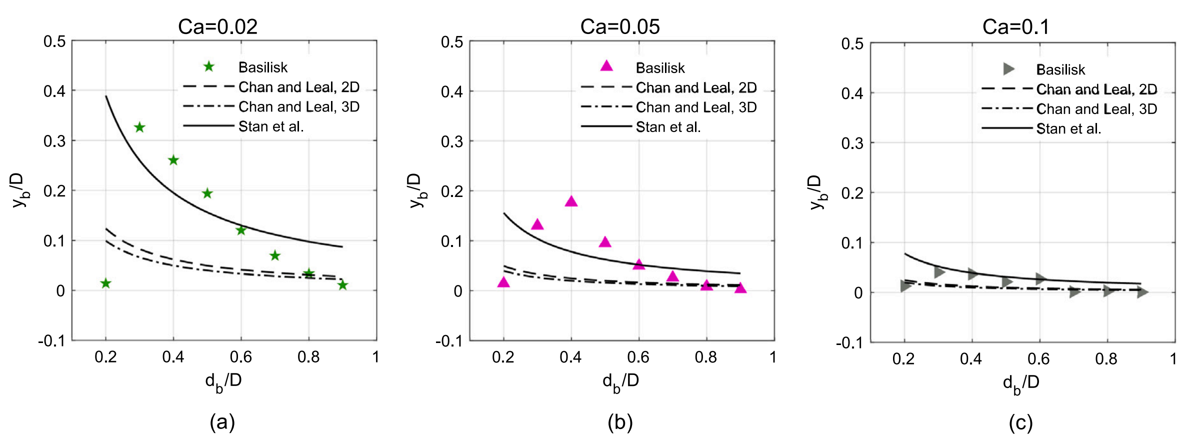

Fig. 7. Vertical position of the centre of mass of the bubble for three selected capillary numbers (Bo = 0.04) and predictions obtained with the models of Chan and Leal (1979) and Stan et al. (2013) for the deformation-induced lift force. (For interpretation of the references to colour in this figure legend, the reader is referred to the web version of this article.)

flows. Predictions of the terminal position of the bubbles y_b/D are obtained by balancing the deformation-induced lift force, estimated via Eq. (3) or Eq. (4), with the buoyancy force estimated via Eq. (2). Eq. (3) from Chan and Leal (1979) is utilised without multiplication by Ca, as Stan et al. (2013) observed that the equation underestimated the lift force by a factor proportional to Ca. Also, Eq. (3) is used with two different expressions for $f(\lambda)$, one calculated for two-dimensional planar Poiseuille flow and one for three-dimensional flow; see Eqs. (6.8) and (6.10) in Chan and Leal (1979). Eq. (4) from Stan et al. (2013) is utilised with $C_L = 200$, which is the mid point of the range $C_L = 100 - 300$ calculated by the authors for bubbles flowing with different fluids and conditions; note that Eq. (4) was derived from experimental data for bubbles travelling near the channel centre ($y_b/D \leq 0.15$) and $d_b/D = 0.25 - 0.5$. The comparison is displayed in Fig. 7. The empirical correlation of Stan et al. (2013) provides reasonable estimations of the bubble positions, although its range of validity is actually rather narrow and the arbitrary choice of C_L is very influential on the predictions. The use of the theoretical model of Chan and Leal (1979), with the correction suggested by Stan et al. (2013), significantly overpredicts the lift force and thus estimates equilibrium bubble positions nearer the pipe axis. If multiplication by Ca was retained in Eq. (3), the predicted values of y_b/D would all be above 0.5, which is nonphysical. Interestingly, the model suggests that the equilibrium positions in the two- and three-dimensional cases are very close, which for objects transported in Poiseuille flows was already observed in previous studies (Feng et al., 1994; Mortazavi and Tryggvason, 2000; Stan et al., 2011) and confirmed by our simulation results presented in Appendix. Note that none of the available models is able to predict the nonmonotonic trend of y_b vs. d_b observed for all capillary numbers as $d_b/D \to 0$ and also reported in previous experimental studies (Khodaparast et al., 2015; Stan et al., 2011). This is due to the simplistic assumptions adopted which give rise to a linear relationship between deformation-induced lift and distance between bubble centre and pipe axis, y_b/D, leading to $y_b/D \propto 1/r_b$.

4.1.2. Bubble dynamics at varying bond number

The results in terms of bubble elevation, speed and shapes for a fixed capillary number of $\mathrm{Ca} = 0.02$ and Bond number varying in the range $\mathrm{Bo} = 0.004 - 0.4$ are presented in Fig. 8. At the lowest values of the Bond number tested, $\mathrm{Bo} = 0.004$ and 0.008, the bubbles appear centred across the entire range of diameters studied $d_b/D = 0.2$–0.9, see Fig. 8(a), and their shape approximates well that of a circle (Fig. 8(c)). The bubble speed exhibits a monotonically increasing trend as the size is reduced, in agreement with the trends previously observed in the case of negligible buoyancy effects (see Fig. 3(e)). When the Bond number is increased to 0.02 to match the value of the capillary number, the bubble elevation increases monotonically from $d_b/D = 0.9$ to 0.4. The corresponding bubble speed increases as d_b is decreased and reaches a local maximum for $d_b = 0.6$, after which further elevation of the bubble causes a dip in speed down to a local minimum identified for $d_b/D = 0.4$. At smaller bubble diameters, the effect of buoyancy weakens, and thus the bubble elevation drops to almost zero at $d_b/D = 0.2$, with the velocity recovering the maximum value at the channel centre. This non-monotonic trend of y_b versus d_b was already observed in Fig. 4(c) for $\mathrm{Bo} = 0.04$ and $\mathrm{Ca} = 0.05$, and therefore suggests that the ratio d_b/D may have an influence on the equilibrium position of the bubble when the capillary number and the Bond number calculated based on the channel diameter are of comparable magnitude. Similar trends are detected for $\mathrm{Bo} = 0.04$ and 0.08, with the bubble elevation progressively reaching the maximum value possible for a bubble travelling along the top wall, accompanied by a gradual decrease in bubble speed as the Bond number grows. At the highest Bond number tested, $\mathrm{Bo} = 0.4$, the limiting case of buoyancy effects dominating over viscous effects is achieved, and the bubbles reach the highest possible elevation. The bubble speed exhibits a maximum for $d_b/D = 0.8$ and then decreases monotonically along the entire range of d_b tested, down to $U_b/U_l \approx 0.6$ when $d_b = 0.2D$. Fig. 8(d) confirms that all bubbles travel near the top wall when $\mathrm{Bo} = 0.4$ and their shape becomes progressively more deformed, relative to a circle, as their size increases. The minimum distance between the top of the bubble and the wall increases from $0.01D$ when $d_b/D \leq 0.5$ to $0.02D$ when $d_b/D \geq 0.8$, in good agreement with the simulation results of Rivero-Rodriguez and Scheid (2018) who predicted a minimum gap thickness of $0.02D - 0.03D$ for off-centred bubbles travelling at $y_b = y_{b,max}$ and $\mathrm{Ca} = 0.02$. In summary, Fig. 8(a) emphasises that the regime transition between bubbles travelling near the channel centre and bubbles being significantly elevated occurs for Bond numbers between $\mathrm{Bo} = 0.008$ and 0.04, which corresponds to the range $\mathrm{Bo/Ca} = 0.4 - 2$, further confirming the relevance of the ratio of Bond and capillary numbers to describe the equilibrium position of the bubble.

Fig. 9 depicts bubble shapes, streamlines and pressure profiles around the bubble for $\mathrm{Ca} = 0.02$ and $\mathrm{Bo} = 0.4$, and different bubble sizes. For $d_b/D = 0.5$, Fig. 9(a), the bubble travels slower than the average liquid speed in the channel and thus liquid bypasses the bubble below it, such that the top and bottom recirculating vortices are separated by this unidirectional stream of liquid. The pressure profile displayed in Fig. 9(d) is qualitatively similar to that depicted in Fig. 5 for $\mathrm{Ca} = 0.005$, since the bubble size and elevation are the same and the velocity field is similar. When the bubble size is increased to $d_b/D = 0.7$, Fig. 9(b), the bubble travels faster ($U_b \approx 1.15U_l$) than the fluid stream below it. The two clockwise rotating vortices on the bottom half of the channel move upwards owing to the lower relative speed between bubble and liquid at the channel centreline, and impinge directly on the bubble surface. Nonetheless, the pressure distribution around the bubble remains similar to that for $d_b/D = 0.5$, with two pressure maxima on the first and third quadrants and two minima on the second and fourth quadrants. When the bubble almost completely occludes the channel cross-section, $d_b/D = 0.9$, the bottom end of the bubble extends beyond the two clockwise recirculating vortices on the bottom half of the channel, and is thus impinged by the near-wall stream of fluid travelling backward. This gives rise to two additional pressure extrema, a local maximum on the fourth quadrant at about $\theta = 295°$ where the near-wall fluid stream impacts the bubble, and a local minimum on the third quadrant ($\theta \approx 250°$) where the streamlines leave the bubble.

4.1.3. Analysis of the entire database

Simulations were performed by systematically varying the Bond number in the range $\mathrm{Bo} = 0.004 - 0.4$. Plots of the bubble elevation and speed at steady-state are presented in Fig. 10 for all values of the Bond number tested. When $\mathrm{Bo} = 0.004$, Fig. 10(a,b), buoyancy effects are weak and bubbles are centred as long as $\mathrm{Ca} \geq 0.005$, i.e. $\mathrm{Bo/Ca} \leq 0.8$. As the capillary number is further reduced to $\mathrm{Ca} = 0.002$ ($\mathrm{Bo/Ca} = 2$), larger bubbles ($d_b/D > 0.6$) that are more sensitive to buoyancy effects begin to appear elevated and travel at a lower speed in the vicinity of the top wall, whereas bubbles with $d_b \leq 0.6$ remain centred. Upon further reduction of the capillary number, $\mathrm{Ca} = 0.0005$, the trends for y_b and U_b versus d_b remain similar but the transition between centred and near-wall travelling bubbles shifts towards smaller bubbles. Therefore, buoyancy effects are gradually overcoming viscous forces as the capillary number decreases, despite the very small Bond number. The buoyancy force becomes dominant over viscous effects throughout the range of d_b for $\mathrm{Ca} = 0.0001$, where all bubbles reach the maximum elevation possible. Note that the bubble speed for $\mathrm{Ca} = 0.0001$ and $d_b = 0.2 - 0.3$ became unstable and thus these two data points are not included in Fig. 10(b). Similar trends versus bubble size and capillary number are observed for $\mathrm{Bo} = 0.008$ in Fig. 10(c,d). Since the magnitude of the buoyancy force is doubled with respect to the previous case, a higher value of the capillary number must be reached, $\mathrm{Ca} = 0.01$, in order for bubbles to remain centred in the channel. When $\mathrm{Ca} < 0.01$, bubbles with larger equivalent diameters are the first to elevate due to buoyancy, whereas smaller bubbles remain centred, further emphasising the importance of the ratio d_b/D on the force balance. As the Bond number is increased to $\mathrm{Bo} = 0.02$ and 0.08, the threshold $\mathrm{Bo/Ca} = 1$ is achieved at progressively larger capillary numbers, where bubble deformation becomes apparent. Therefore, while for small Bond numbers the equilibrium position of the bubble is either $y_b \approx 0$ or $y_b \approx y_{b,max}$, at larger Bond numbers the deformation-induced lift force yields equilibrium positions that distribute uniformly between these two limiting values. Note that as the capillary number is increased, the

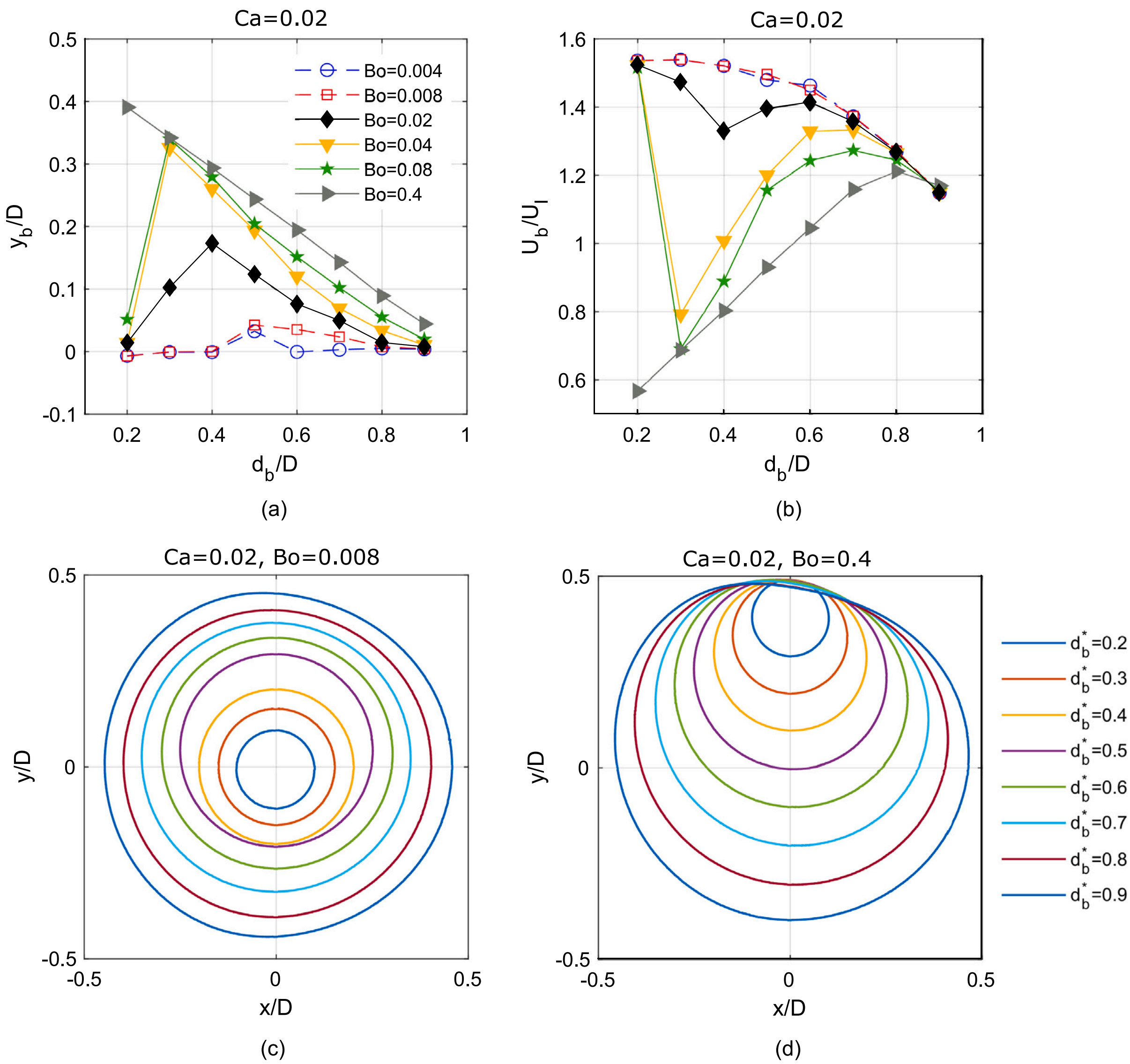

Fig. 8. Analysis of the effect of the Bond number on the (a) bubble elevation and (b) speed at constant $\mathrm{Ca} = 0.02$. Full symbols and solid lines are used for datapoints with $\mathrm{Bo}/\mathrm{Ca} \geq 1$, whereas empty symbols and dashed lines are used for datapoints with $\mathrm{Bo}/\mathrm{Ca} < 1$. (c,d) Bubble shapes at varying bubble diameter and Bond number. (For interpretation of the references to colour in this figure legend, the reader is referred to the web version of this article.)

bubble speed for $d_b/D \to 1$ increases to values above $U_b/U_l = 1$, because the bubble becomes elongated and hence its velocity approaches Bretherton's law, $U_b/U_l \sim 1/(1 - \mathrm{Ca}^{2/3})$ (Bretherton, 1961). At the highest value of the Bond number tested, $\mathrm{Bo} = 0.4$, a capillary number above 0.2 is necessary for bubbles to remain centred and significant bubble deformation occurs. At $\mathrm{Bo} = 0.4$ and $\mathrm{Ca} = 0.5$, the bubble speed is nearly $U_b = 1.5U_l$ and becomes almost independent of its size.

In summary, the trends of bubble elevation versus d_b/D displayed in Fig. 10 at varying Bond numbers are all quite similar, with y_b ranging from close to zero to $y_{b,max} = (D - d_b)/2$, depending on Bond number, capillary number and bubble size. The ratio Bo/Ca is effective in predicting the transition from centred to near-wall bubbles, which is justified by the fact that the vertical position of the bubble at equilibrium is a result of the competition between the buoyancy force, proportional to Bo, and the deformation-induced lift force, which scales with the viscous shear and is thus proportional to Ca. Note that the relevance of the group Bo/Ca in describing the competition between buoyancy and viscous forces on the flow emerges also from nondimensionalisation of the momentum Eq. (7). Using U_l as a velocity scale, D as a length scale and $\mu_l U_l/D$ as a pressure scale, the Stokes flow equations at steady-state read as follows:

$$-\hat{\nabla}\hat{p} + \hat{\nabla} \cdot \left[(\hat{\nabla}\hat{\boldsymbol{u}} + \hat{\nabla}^T \hat{\boldsymbol{u}}) \right] - \frac{\rho}{\rho_l} \frac{\mathrm{Bo}}{\mathrm{Ca}} \hat{\boldsymbol{j}} + \frac{1}{\mathrm{Ca}} \hat{\kappa} \boldsymbol{n} \hat{\delta}_s = 0 \tag{9}$$

with $\hat{p} = p/(\mu_l U_l/D)$, $\hat{\boldsymbol{x}} = \boldsymbol{x}/D$, $\hat{\boldsymbol{u}} = \boldsymbol{u}/U_l$, $\hat{\kappa} = \kappa D$ and $\hat{\delta}_s = \delta_s D$; $\hat{\boldsymbol{j}}$ denotes the unit vector in the y direction. The buoyancy term in the equation above is multiplied by the factor Bo/Ca, further confirming that the impact of the body force is modulated by viscous effects.

To correctly account for the dependence of the buoyancy force on the bubble size, and hence capture the non-monotonic trends of y_b/D versus d_b/D observed when Bo/Ca is on the order of 1, e.g., those reported in Fig. 10(e) for $\mathrm{Ca} = 0.02$, the Bond number should be calculated based on the bubble diameter, $\mathrm{Bo_b} = \rho_l g d_b^2/\sigma = \mathrm{Bo}\,(d_b/D)^2$, rather than the channel diameter. Therefore, the nondimensional group $\mathrm{Bo}\,(d_b/D)^2/\mathrm{Ca}$ is expected to be the most appropriate parameter to assess the importance of buoyancy on the dynamics of small bubbles travelling in horizontal microchannels.

To verify this hypothesis, all data for the bubble elevation, rescaled by the maximum elevation possible depending on d_b ($y_{b,max} = (D - d_b)/2$), are plotted in Fig. 11 as a function of the identified group

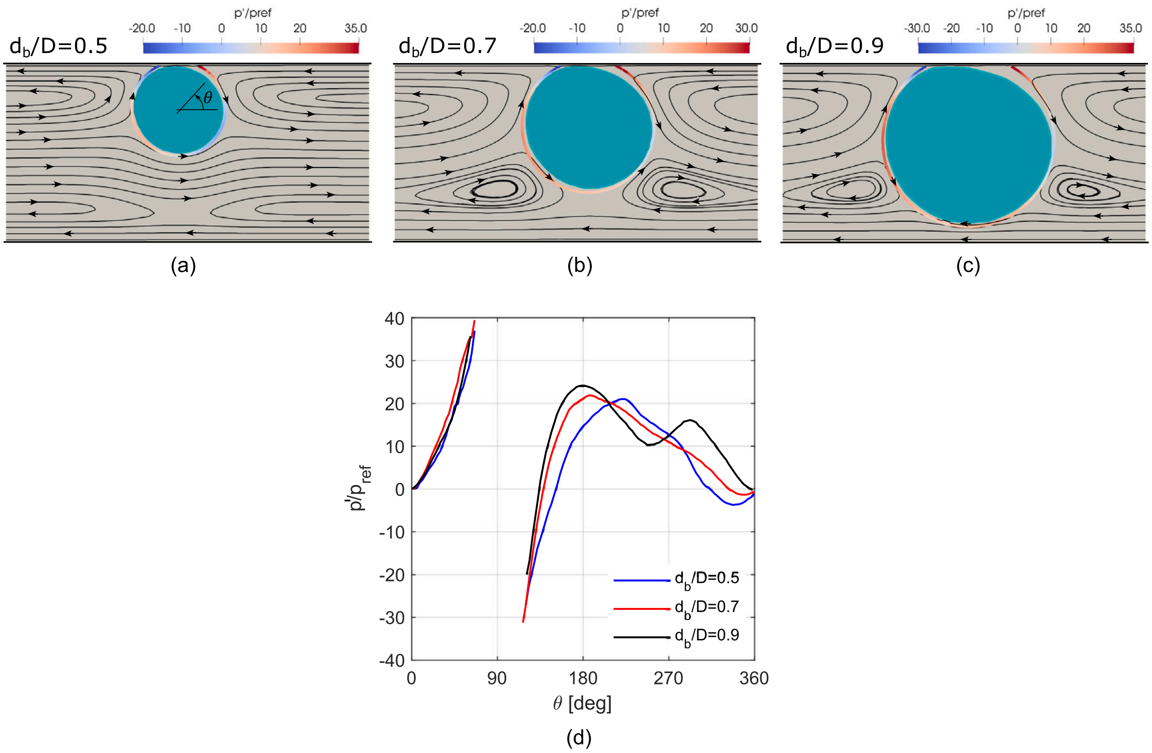

Fig. 9. (a,b,c) Bubble shape, streamlines and circumferential pressure distributions around the bubble for Ca = 0.02 and Bo = 0.4 and three selected bubble sizes; streamlines are shown in a reference frame moving with the bubble; pressure values are reported at the net of the hydrostatic head, $p' = p - \rho_l g(R-y)$, and are rescaled with a pressure reference calculated as $p_{ref} = \mu_l U_l / D$. (d) Circumferential pressure profiles extracted on the circles around the bubbles depicted in (a,b,c). (For interpretation of the references to colour in this figure legend, the reader is referred to the web version of this article.)

$\mathrm{Bo}\,(d_b/D)^2/\mathrm{Ca}$. Data are displayed with different colours and symbols depending on their Bond number in Fig. 11(a), and on the bubble-to-channel diameter ratio $d_b^* = d_b/D$ in Fig. 11(b). The database contains 312 datapoints, for Bo = 0.004–0.4, Ca = 10^{-4}–0.5 and $d_b/D = 0.2$–0.9. Although scattered, the datapoints distribute along a diagonal centred at $\mathrm{Bo}\,(d_b/D)^2/\mathrm{Ca} = 1$, with $y_b/y_{b,max} < 0.2$ when $\mathrm{Bo}\,(d_b/D)^2/\mathrm{Ca} < 0.1$ and thus viscous effects overcome buoyancy, whereas $y_b/y_{b,max} > 0.8$ when $\mathrm{Bo}\,(d_b/D)^2/\mathrm{Ca} > 10$ and buoyancy dominates. To quantify the performance of the threshold criterion $\mathrm{Bo}\,(d_b/D)^2/\mathrm{Ca} = 1$ in determining the importance of buoyancy effects, we separate the datapoints characterised by values of $\mathrm{Bo}\,(d_b/D)^2/\mathrm{Ca}$ below 1 from those that have values above 1. For the first group of points, buoyancy effects are expected to be weak, and thus the bubble elevation should be below $0.5y_{b,max}$. For the second group of points, buoyancy is expected to overcome other forces, and thus the bubble elevation should be above $0.5y_{b,max}$. These two regimes are displayed as light green regions in Fig. 11. If the threshold $\mathrm{Bo}\,(d_b/D)^2/\mathrm{Ca} = 1$ was exact in predicting the transition between the two regimes, all datapoints should lay within the green zones. The percentage of datapoints falling within these two quadrants is 81.4%, thus confirming that the suggested criterion is effective in predicting the impact of buoyancy on the equilibrium position of the bubble. The criterion is equally effective in predicting both regimes. Of the 180 datapoints that have $y_b/y_{b,max} < 0.5$, 157 points (87%) have $\mathrm{Bo}\,(d_b/D)^2/\mathrm{Ca} < 1$; of the remaining 132 datapoints with $y_b/y_{b,max} > 0.5$, 99 points (75%) have $\mathrm{Bo}\,(d_b/D)^2/\mathrm{Ca} \geq 1$. The datapoints that lay outside the green quadrants in Fig. 11 (less than 20% of the database) refer to conditions where the bubble is more centred than expected despite being characterised by $\mathrm{Bo}\,(d_b/D)^2/\mathrm{Ca} > 1$ (bottom-right quadrant), or the bubble is more elevated than expected despite having $\mathrm{Bo}\,(d_b/D)^2/\mathrm{Ca} < 1$ (top-left quadrant). Most of the points in the bottom-right quadrant have Bo ≥ 0.04, $d_b/D \geq 0.8$ and Ca > 0.01. Hence, these are large bubbles for which $y_{b,max} \leq 0.1D$ and therefore a small change in y_b induces a large change in $y_b/y_{b,max}$. Most of the points in the top-left quadrant have Bo ≥ 0.02, $d_b/D \leq 0.5$ and Ca > 0.01. These are small bubbles for which the ratio $(d_b/D)^2$ becomes very small, hence it is plausible that the exponent of the diameter ratio needs adjustment to avoid skewing the data towards the regime of negligible buoyancy effects; we have verified that these data would be predicted well using an exponent of one.

The suggested criterion assesses the importance of buoyancy effects according to the ratio $\mathrm{Bo_b}/\mathrm{Ca} = \rho_l g d_b^2/(\mu_l U_l)$, and thus regards the deformation-induced lift force caused by viscous shear as the only force opposing buoyancy. This does not mean that surface tension is disregarded by this method. Since both $\mathrm{Bo_b}$ and Ca are much smaller than unity, surface tension is actually the dominant force in the flow and its main effect is to preserve the spherical shape of the bubble. The equilibrium position of the bubble within the channel is then determined by the competition between the remaining forces, i.e. buoyancy and viscous shear, which are at least an order of magnitude smaller than surface tension.

4.2. Flows with inertial effects

Inertial effects on the trajectory of small particles, bubbles and droplets transported within microchannels become non-negligible already for Reynolds numbers on the order of 1 (Di Carlo et al., 2009; Stan et al., 2011; Zhang et al., 2016; Hadikhani et al., 2018). For elongated bubbles, with $d_b/D > 1$, inertial effects become apparent when the Weber number of the flow, We = Ca Re, grows above 0.1, and act by changing the shape of the front and rear menisci of the bubbles (Magnini et al., 2017b,a). For small bubbles ($d_b/D < 1$) travelling near the channel centre, inertia tends to push the bubble towards the wall (Stan et al., 2011). However, the interplay of inertia and deformation-induced lift force when a bubble travels far from the centre is still unclear. Hence, in this section the impact of inertia on the bubbles shapes and dynamics are assessed by considering Reynolds

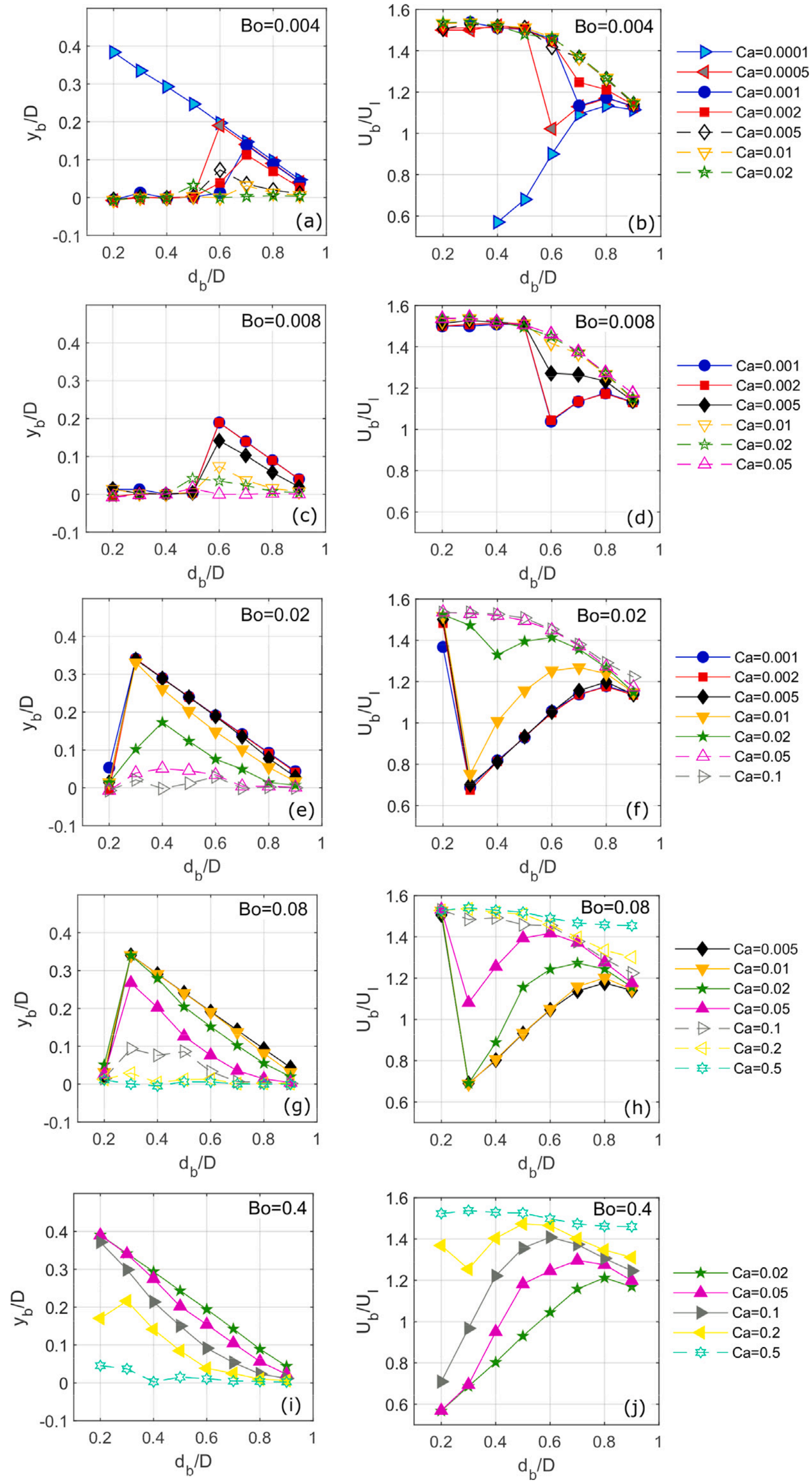

Fig. 10. Vertical positions of centre of mass of the bubble and bubble speed for all remaining Bond numbers tested. Full symbols and solid lines are used for datapoints with $\mathrm{Bo/Ca} \geq 1$, whereas empty symbols and dashed lines are used for datapoints with $\mathrm{Bo/Ca} < 1$. (For interpretation of the references to colour in this figure legend, the reader is referred to the web version of this article.)

numbers within the range $\mathrm{Re} = 1 - 100$, capillary numbers within $\mathrm{Ca} = 0.001 - 0.1$, and a Bond number fixed to $\mathrm{Bo} = 0.04$. The results of the simulations, including equilibrium position, velocity and shape of the bubbles, are presented in Fig. 12. The data corresponding to $\mathrm{Re} = 0$ (Stokes flow regime) and discussed in Section 4.1 are also included in the figure for comparison.

For $\mathrm{Ca} = 0.001$, increasing the Reynolds number up to 100 has no appreciable effect. Owing to the relatively large Bond number and small capillary number ($\mathrm{Bo/Ca} = 40$), bubbles travel near the top wall of the channel and remain spherical across the range of Re tested. At the end of Section 2, it was discussed that the relevant nondimensional group quantifying the competition of buoyancy and inertial forces is Bo/We, which takes the values 0.4 – 40 in the conditions studied ($\mathrm{Ca} = 0.001$) thus explaining the weak effect of inertia over buoyancy. Furthermore, the Weber number of the flow remains below 0.1 and thus inertia is also not sufficient to alter the shape of the bubbles.

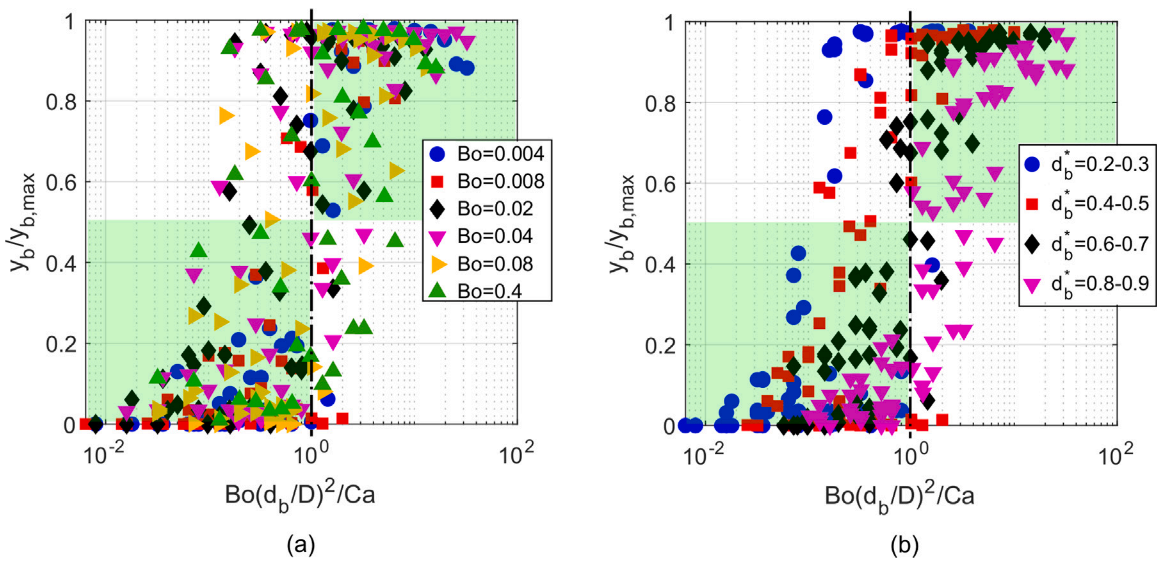

Fig. 11. Elevation of the centre of mass of the bubble, rescaled by its maximum possible value $y_{b,max} = (D - d_b)/2$, plotted as a function of the identified governing parameter for buoyancy effects. (a) Datapoints are classified by the value of the Bond number. (b) Datapoints are classified by the value of the nondimensional bubble diameter, $d_b^* = d_b/D$. The vertical dash-dotted lines in both figures identify the threshold $\mathrm{Bo}(d_b/D)^2/\mathrm{Ca} = 1$. The green regions in the graphs identify the quadrants where $\mathrm{Bo}(d_b/D)^2/\mathrm{Ca} < 1$ and $y_b/y_{b,max} < 0.5$, or $\mathrm{Bo}(d_b/D)^2/\mathrm{Ca} > 1$ and $y_b/y_{b,max} > 0.5$. (For interpretation of the references to colour in this figure legend, the reader is referred to the web version of this article.)

When $\mathrm{Ca} = 0.02$, increasing the Reynolds number has only a minor effect on the bubble transversal position, but a more apparent impact on its speed and shape. Bubbles with $d_b/D \geq 0.5$, which are already elevated in the Stokes flow regime, get slightly closer to the top wall of the channel and their speed correspondingly decreases. There is a noticeable change in bubble shapes for $\mathrm{Re} = 100$ and $d_b/D = 0.8 - 0.9$, see Fig. 12(h), with two high interface curvature regions appearing at the top and bottom points of the bubble, where the interface is the closest to the wall. The change in shape is consistent with the Weber number of the flow, i.e. $\mathrm{We} = 2$ for $\mathrm{Re} = 100$. These profiles are qualitatively similar to those imaged by Khodaparast et al. (2015) for air bubbles flowing in water at $\mathrm{Re} > 10$. Note that $\mathrm{Bo/We} = 0.02 - 2$ here, and thus it is expected that inertial effects become comparable to buoyancy as the Reynolds number is increased.

Remarkable inertial effects arise when the Reynolds number is increased for $\mathrm{Ca} = 0.1$, with $\mathrm{Bo/We} = 0.004 - 0.4$. In the absence of inertia, the bubbles travel centred ($y_b/D \geq 0.04$) as the deformation-induced lift overcomes buoyancy. However, inertial forces act by significantly displacing the bubble off the channel axis, up to $|y_b|/D \approx 0.25$ when $d_b/D = 0.3 - 0.5$ with $\mathrm{Re} = 100$, in agreement with previous observations (Di Carlo et al., 2009; Hadikhani et al., 2018). Interestingly, the unopposed inertial force does not seem to push the bubble towards a specific wall, and thus bubbles travelling near the bottom wall are also observed, e.g. $d_b/D = 0.4 - 0.5$ for $\mathrm{Re} = 100$. A set of simulations with the same Ca and $\mathrm{Re} = 100$, but without gravity force ($\mathrm{Bo} = 0$, not shown here), was also performed and returned the same bubble shapes and magnitudes of $|y_b|$; this confirmed that buoyancy effects are negligible under these conditions, and thus inertia alone is responsible for displacing small bubbles off-centre. The bubble shapes also become considerably different from the Stokes flow regime when $\mathrm{Re} = 100$, owing to the high Weber number ($\mathrm{We} = 10$), and thus reduced importance of surface tension. The smaller bubbles that travel near the wall ($d_b/D \leq 0.5$) lean in the direction of the flow, whereas larger bubbles ($d_b/D \geq 0.6$) remain centred and become elongated although being smaller than the channel size, which was also observed in the experiments of Khodaparast et al. (2015) for air–water flows at high flow rates. Notably, the minimum distance between the bubbles and the wall for $\mathrm{Re} = 100$ remains approximately constant across a wide range of bubble sizes ($d_b/D = 0.4 - 0.9$), about $0.08D$, which compares well with the value calculated using the correlation of Aussillous and Quéré (2000) to predict the liquid film thickness h around elongated bubbles, $h/D = 0.67\mathrm{Ca}^{2/3}/(1 + 3.35\mathrm{Ca}^{2/3}) = 0.084$. Note also that, as bubbles elongate, their speed approaches the asymptotic value $U_b/U_l = 1/(1 - 2h/D)$ (Bretherton, 1961) ($U_b/U_l = 1/(1 - 2h/D)^2$ in an axisymmetric geometry), which for $h = 0.08D$ yields $U_b/U_l = 1.2$ and thus motivates the decreasing trend observed for U_b/U_l in Fig. 12(f) when increasing Re at $d_b/D \geq 0.6$.

Fig. 13 displays the bubble shapes, streamlines and pressure contours for $\mathrm{Ca} = 0.1$, $\mathrm{Bo} = 0.04$ and $\mathrm{Re} = 100$. The pressure values are reported not only at the net of the hydrostatic head but, to better reveal the pressure field around the bubbles, the average pressure drop along the channel $\Delta p/L$ is also subtracted, so that $p' = p - \rho_l g(R - y) + x(\Delta p/L)$. Values are then rescaled by the inertial pressure scale, $p_{ref} = \rho_l U_l^2$. The zero pressure reference is now located in the point of minimum pressure around the bubble. In the small bubble case, $d_b/D = 0.3$, the pressure field exhibits the same minima and maxima in the four quadrants around the bubble as observed previously for the Stokes flow regime. When $d_b/D = 0.5$, the bubble deforms considerably owing to the strong inertial effects and the pressure minimum is identified in the correspondence of the high interface curvature region near the channel wall. When $d_b/D = 0.8$ the bubble travels centred in the channel and shows a nearly symmetric profile, with high interface curvature regions near the wall, where the fluid travelling backward and bypassing the bubble accelerates when squeezed between bubble and wall, giving rise to low pressure regions. Between these regions and the bubble nose, the bubble profile is nearly flat and therefore high pressure regions form due to a reduction in the Laplace pressure jump across the liquid–gas interface.

In summary, inertial effects begin to affect the equilibrium position of the bubble when $\mathrm{Bo/We} < 1$, causing small displacements from the position attained in the Stokes flow regime. However, inertia exhibits a significant impact when $\mathrm{We} > 1$ and $\mathrm{Bo/We} < 0.1$, and it manifests by elongating the bubbles of dimensions approaching that of the channel, while making small bubbles migrate towards the channel walls. The latter should not be ascribed to buoyancy effects, since buoyancy forces are more than one order of magnitude smaller than inertia in this regime.

5. Conclusions

In this article, we have shown that buoyancy effects may impact the dynamics and equilibrium positions of bubbles transported by a

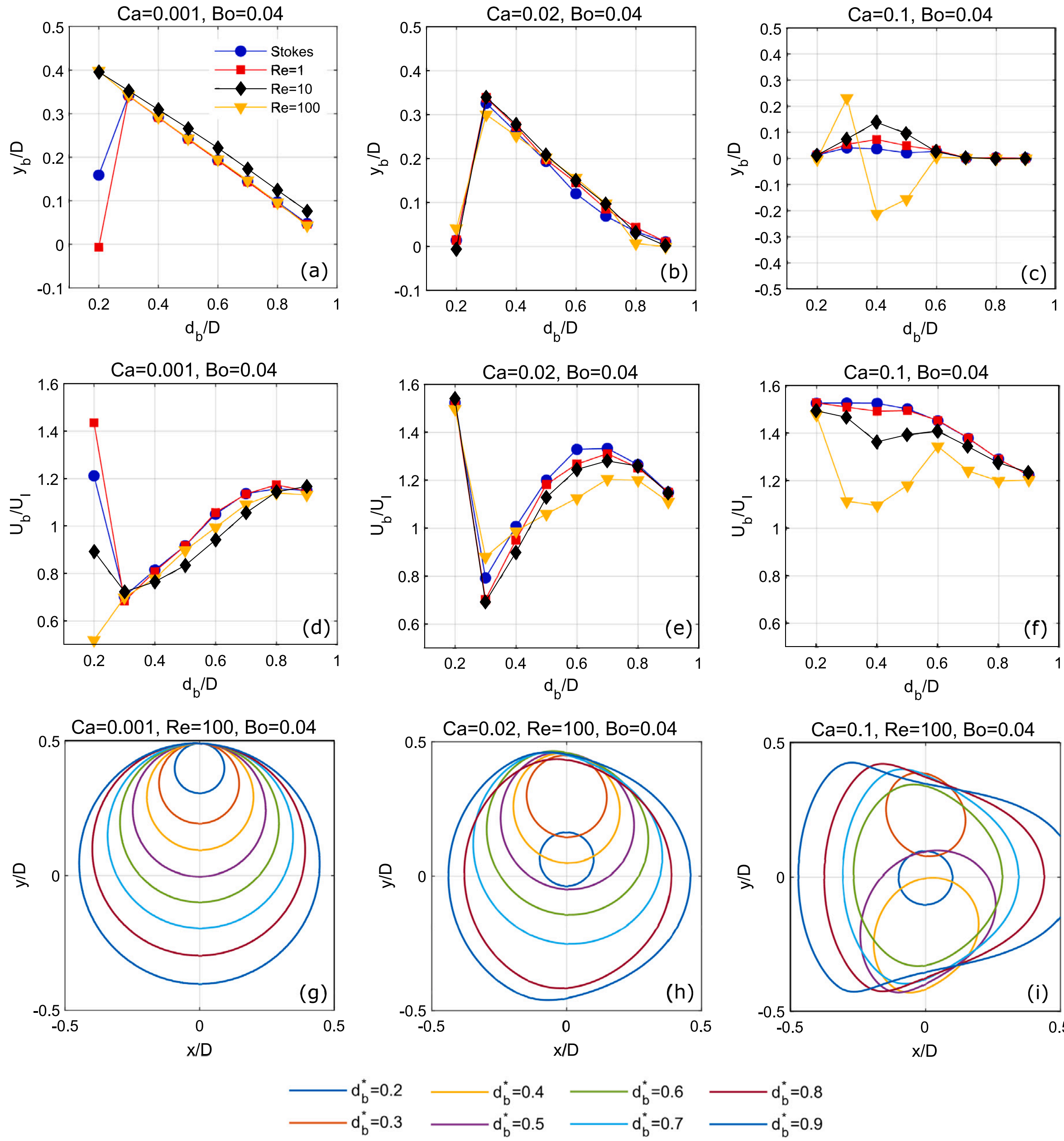

Fig. 12. Effect of the Reynolds number in the (a,b,c) vertical positions of centre of mass of the bubble and (d,e,f) bubble speed, for selected values of the capillary number and Bo = 0.04. (g,h,i) Bubble shapes for selected capillary numbers, Re = 100 and Bo = 0.04. The datapoints for Stokes flow in (a-f) are those obtained disregarding the convective term in Eq. (7) and discussed in Section 4.1. (For interpretation of the references to colour in this figure legend, the reader is referred to the web version of this article.)

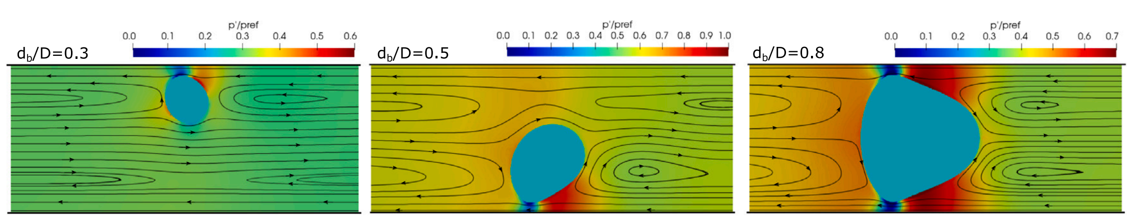

Fig. 13. Bubble shapes, streamlines and contours of pressure for Ca = 0.1, Bo = 0.04 and Re = 100. Streamlines are shown in a reference frame moving with the bubble; the pressure values are reported at the net of the hydrostatic head and of the streamwise pressure drop in the channel, $p' = p - \rho_l g(R - y) + x(\Delta p/L)$, and are rescaled with a pressure reference calculated as $p_{ref} = \rho_l U_l^2$. (For interpretation of the references to colour in this figure legend, the reader is referred to the web version of this article.)

liquid flow in a horizontal microchannel, even when the Bond number is much smaller than one. This is due to the fact that, if the capillary and Reynolds numbers of the flow are small, inertial and viscous forces cannot generate a cross-stream force that is sufficiently strong to oppose gravity. Therefore, the bubble elevates above the channel centre and achieves an equilibrium position whose distance from the wall depends on the relative magnitude of these forces. Using direct numerical simulations performed with the free software Basilisk, we have generated a database of bubble equilibrium positions within the channel covering a wide range of conditions, $\mathrm{Bo} = 0.004-0.4$, $\mathrm{Ca} = 10^{-4}-0.5$, $\mathrm{Re} = 0-100$, and $d_b/D = 0.2-0.9$. Since surface tension does not directly impact the equilibrium position of the bubble, the Bond number alone is not sufficient to describe the bubble trajectory. The role of buoyancy should be therefore assessed against the deformation-induced lift force, which originates from the viscous shear at the bubble interface and is described by the capillary number. We have thus identified the nondimensional group $\mathrm{Bo}\,(d_b/D)^2/\mathrm{Ca}$ as the most effective in assessing buoyancy effects for flows with negligible inertial forces. When $\mathrm{Bo}\,(d_b/D)^2/\mathrm{Ca} < 0.1$, buoyancy effects are negligible and the bubble travels along the axis of the channel. When $\mathrm{Bo}\,(d_b/D)^2/\mathrm{Ca} > 10$, buoyancy effects dominate and the bubble travels in the vicinity of the top wall. For intermediate values, bubbles take equilibrium positions between channel centre and wall, and the threshold $\mathrm{Bo}\,(d_b/D)^2/\mathrm{Ca} = 1$ is effective in predicting whether the bubbles will travel closer to the channel centre or to the wall. Inertial forces begin impacting the shape of the bubble when $\mathrm{We} > 1$ and significantly alter their equilibrium positions when $\mathrm{Bo}/\mathrm{We} < 1$. Under the action of inertia, bubbles of size comparable to the channel diameter become elongated, whereas smaller bubbles migrate towards the channel wall. The latter effect does not depend on buoyancy, and thus the bubbles do not exhibit a preferential near-wall circumferential position.

CRediT authorship contribution statement

Jakub A. Cranmer: Writing – original draft, Visualization, Validation, Methodology, Investigation, Formal analysis. **Evgenii Sharaborin:** Writing – review & editing, Supervision, Software, Methodology. **Sepideh Khodaparast:** Writing – review & editing, Investigation, Formal analysis, Conceptualization. **Giovanni Giustini:** Writing – review & editing, Supervision, Funding acquisition. **Mirco Magnini:** Writing – review & editing, Writing – original draft, Validation, Supervision, Resources, Project administration, Investigation, Funding acquisition, Formal analysis, Data curation, Conceptualization.

Declaration of competing interest

The authors declare that they have no known competing financial interests or personal relationships that could have appeared to influence the work reported in this paper.

Acknowledgements

M. Magnini and G. Giustini acknowledge support from the UK Engineering & Physical Sciences Research Council (EPSRC), via grants EP/T033398/1 and EP/T027061/2, respectively. Calculations were performed using the Sulis Tier-2 HPC platform hosted by the Scientific Computing Research Technology Platform at the University of Warwick, which has been funded by EPSRC, United Kingdom (grant number EP/T022108/1) and the HPC Midlands + consortium.

Appendix. Comparison of 2D and 3D simulations

Three-dimensional simulations for a few selected cases were performed to verify the results, in terms of equilibrium positions of the bubbles, obtained with the two-dimensional planar simulations. The conditions studied refer to those discussed in Section 4.1.1, $\mathrm{Bo} = 0.04$ and Stokes flow ($\mathrm{Re} = 0$). The capillary numbers tested with 3D simulations were $\mathrm{Ca} = 0.001, 0.05$ and 0.1, so that all regimes were achieved, from bubbles travelling near the top wall subjected to important buoyancy effects ($\mathrm{Ca} = 0.001$), to bubbles travelling near the centreline with minor buoyancy effects ($\mathrm{Ca} = 0.1$). The 3D simulations were run using a grid with a maximum level of refinement of 10, i.e. 50 cells across the channel diameter, except for $d_b/D = 0.2$ which was run with a level of refinement of 11 to ensure that at least 20 cells discretised the bubble along its diameter. A mesh convergence analysis was performed by testing finer meshes with maximum levels of refinement of 11 and 12, however, the differences in the steady-state transversal positions of the bubbles were negligible.

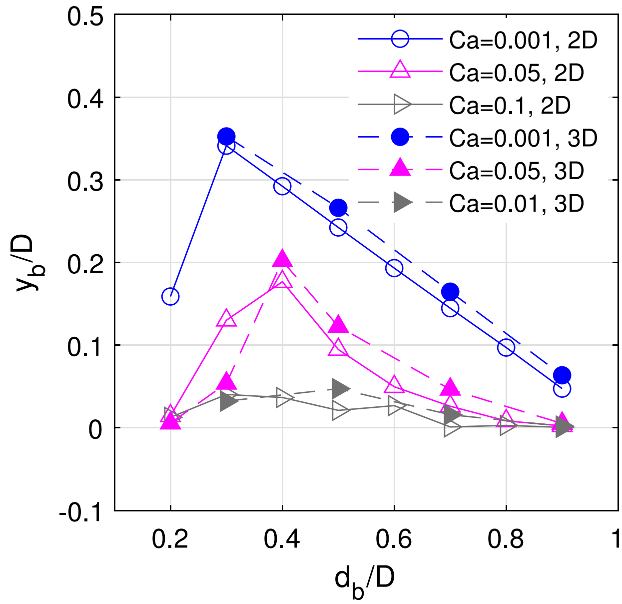

Fig. A.1. Comparison of 2D and 3D simulation results for $\mathrm{Bo} = 0.04$ and Stokes flow ($\mathrm{Re} = 0$). The figure shows the vertical position of the centre of mass of the bubble versus bubble size. The 2D data correspond to those plotted in Fig. 4(b). (For interpretation of the references to colour in this figure legend, the reader is referred to the web version of this article.)

The comparison of the equilibrium positions achieved by the bubbles is shown in Fig. A.1. It can be seen that the difference in the steady-state positions is small and remains within a few percent of the diameter of the channel. In the case of $\mathrm{Ca} = 0.001$, the bubbles in the 3D simulations are slightly closer to the top wall because the liquid layer separating them from the wall is under-resolved. Overall, the equilibrium positions between 2D and 3D simulations agree well, providing confidence that the new criterion proposed to assess the buoyancy effects, validated against a databank of 2D simulation results, is applicable also for the 3D configuration. A similar agreement between equilibrium positions of objects transported in Poiseuille flows in planar 2D and circular 3D configurations was already reported by Feng et al. (1994) for solid particles, Mortazavi and Tryggvason (2000) for droplets and Stan et al. (2011) for bubbles.

The two-dimensional simulations are significantly cheaper than the three-dimensional simulations in terms of computational time. For example, considering as representative the conditions $\mathrm{Ca} = 0.05$, $\mathrm{Bo} = 0.04$, Stokes flow, and $d_b/D = 0.4$, the two-dimensional simulation run with a maximum level of refinement of 11 and a channel length of $80D$ required 1152 CPU hours (12 days using 4 parallel cores) to achieve steady-state. The corresponding three-dimensional simulation with level 10 and same channel length required about 86,000 CPU hours (14 days using 256 cores).

Data availability

Data will be made available on request.

References

Atasi, O., Khodaparast, S., Scheid, B., Stone, H.A., 2021. Effect of buoyancy on the motion of long bubbles in horizontal tubes. Phys. Rev. Fluids 2, 094304.

Aussillous, P., Quéré, D., 2000. Quick deposition of a fluid on the wall of a tube. Phys. Fluids 12, 2367–2371.
Bell, J.B., Colella, P., Glaz, H.M., 1989. A second-order projection method for the incompressible navier-stokes equations. J. Comput. Phys. 85, 257–283.
Brauner, N., Moalem Maron, D., 1992. Stability analysis of stratified liquid-liquid flow. Int. J. Multiph. Flow 18, 103–121.
Bretherton, F.P., 1961. The motion of long bubbles in tubes. J. Fluid Mech. 10, 166–188.
Cappello, J., Rivero-Rodriguez, J., Vitry, Y., Dewandre, A., Sobac, B., Scheid, B., 2023. Beads, bubbles and drops in microchannerls: stability of centred position and equilibrium velocity. J. Fluid Mech. 956, A21.
Chan, C.H., Leal, L.G., 1979. The motion of a deformable drop in a second-order fluid. J. Fluid Mech. 92, 131–170.
Chen, X., Xue, C., Zhang, L., Hu, G., Jiang, X., Sun, J., 2014. Inertial migration of deformable droplets in a microchannel. Phys. Fluids 26, 112003.
Di Carlo, D., Edd, J.F., Humphry, K.J., Stone, H.A., Toner, M., 2009. Particle segregation and dynamics in confined flows. Phys. Rev. Lett. 102, 094503.
Di Carlo, D., Irimia, D., Tompkins, R.G., Toner, M., 2007. Continuous inertial focusing, ordering, and separation of particles in microchannels. Proc. Natl. Acad. Sci. USA 104, 18892.
Feng, J., Hu, H.H., Joseph, D.D., 1994. Direct simulation of initial value problems for the motion of solid bodies in a Newtonian fluid. Part 2. Couette and Poiseuille flows. J. Fluid Mech. 277, 271–301.
Garstecki, P., Gitlin, I., DiLuzio, W., Whitesides, G., Kumacheva, E., Stone, H.A., 2004. Formation of monodisperse bubbles in a microfluidic flow-focusing device. Appl. Phys. Lett. 85, 2649–2651.
Hadikhani, P., Hashemi, S.M.H., Balestra, G., Zhu, L., Modestino, M.A., Gallaire, F., Psaltis, D., 2018. Inertial manipulation of bubbles in rectangular microfluidic channels. Lab Chip 18, 1035–1046.
Hashemi, S.M.H., Modestino, M.A., Psaltis, D., 2015. A membraneless electrolyzer for hydrogen production across the pH scale. Energy Environ. Sci. 8, 2003–2009.
Hur, S.C., Henderson-MacLennan, N.K., McCabe, E.R.B., Di Carlo, D., 2011. Deformability-based cell classification and enrichment using inertial microfluidics. Lab Chip 11, 912–920.
Hyman, W.A., Skalak, R., 1972. Viscous flow of a suspension of liquid drops in a cylindrical tube. Appl. Sci. Res. 26, 27–52.
Karayiannis, T.G., Mahmoud, M.M., 2017. Flow boiling in microchannels: Fundamentals and applications. Appl. Therm. Eng. 115, 1372–1397.
Kew, P.A., Cornwell, K., 1997. Correlations for prediction of flow boiling heat transfer in small-diameters channels. Appl. Therm. Eng. 17, 705–715.
Khodaparast, S., Magnini, M., Borhani, N., Thome, J.R., 2015. Dynamics of isolated confined air bubbles in liquid flows through circular microchannels: an experimental and numerical study. Microfluid Nanofluid 19, 209–234.
Magnaudet, J., Takagi, S., Legendre, D., 2003. Drag, deformation and lateral migration of a buoyant drop moving near a wall. J. Fluid Mech. 476, 115–157.
Magnini, M., Beisel, A., Ferrari, A., Thome, J.R., 2017a. Pore-scale analysis of the minimum liquid film thickness around elongated bubbles in confined gas-liquid flows. Adv. Water Resour. 109, 84–93.
Magnini, M., Ferrari, A., Thome, J.R., Stone, H.A., 2017b. Undulations on the surface of elongated bubbles in confined gas-liquid flows. Phys. Rev. Fluids 2, 084001.
Magnini, M., Khodaparast, S., Matar, O.K., Thome, J.R., Stone, H.A., 2019. Dynamics of long gas bubbles rising in a vertical tube in a cocurrent liquid flow. Phys. Rev. Fluids 4, 023601.
Moran, H., Magnini, M., Markides, C.N., Matar, O.K., 2021. Inertial and buoyancy effects on the flow of elongated bubbles in horizontal channels. Int. J. Multiph. Flow 135, 103468.
Mortazavi, S., Tryggvason, G., 2000. A numerical study of the motion of drops in Poiseuille flow. Part 1. Lateral migration of one drop. J. Fluid Mech. 411, 325–350.
Municchi, F., Markides, C.N., Matar, O.K., Magnini, M., 2024. Computational study of bubble, thin-film dynamics and heat transfer during flow boiling in non-circular microchannels. Appl. Therm. Eng. 238, 122039.
Ong, C.L., Thome, J.R., 2011. Macro-to-microchannel transition in two-phase flow: Part 1 - Two-phase flow patterns and film thickness measurements. Exp. Therm. Fluid Sci. 35, 37–47.
Popinet, S., 2009. An accurate adaptive solver for surface-tension-driven interfacial flows. J. Comput. Phys. 228, 5838–5866.
Popinet, S., 2015. A quadtree-adaptive multigrid solver for the Serre-Green-Naghdi equations. J. Comput. Phys. 302, 336–358.
Rivero-Rodriguez, J., Scheid, B., 2018. Bubble dynamics in microchannels: inertial and capillary migration forces. J. Fluid Mech. 842, 215–247.
Sharaborin, E.L., Rogozin, O.A., Kasimov, A.R., 2021a. Computational study of the dynamics of the Taylor bubble. Fluids 6, 389.
Sharaborin, E.L., Rogozin, O.A., Kasimov, A.R., 2021b. The coupled volume of fluid and Brinkman penalization methods for simulation of incompressible multiphase flows. Fluids 6, 334.
Stan, C.A., Ellerbee, A.K., Guglielmini, L., Stone, H.A., Whitesides, G.M., 2013. The magnitude of lift forces acting on drops and bubbles in liquids flowing inside microchannels. Lab Chip 13, 365–376.
Stan, C.A., Guglielimini, L., Ellerbee, A.K., Caviezel, D., Stone, H.A., Whitesides, G.M., 2011. Sheathless hydrodynamic positioning of buoyant drops and bubbles inside microchannels. Phys. Rev. E 84, 036302.
Triplett, K.A., Ghiaasiaan, S.M., Abdel-Khalik, S.I., Sadowski, D.L., 1999. Gas-liquid two-phase flow in microchannels Part I: two-phase flow patterns. Int. J. Multiph. Flow 25, 377–394.
Ullmann, A., Brauner, N., 2007. The prediction of flow pattern maps in minichannels. Multiph. Sci. Technol. 19, 49–73.
Yang, L., Tan, J., Wang, K., Luo, G., 2014. Mass transfer characteristics of bubbly flow in microchannels. Chem. Eng. Sci. 109, 306–314.
Youngs, D.L., 1982. Time-dependent multi-material flow with large fluid distortion. In: Morton, K.W., Baines, M.J. (Eds.), Numerical Methods for Fluid Dynamics. Academic Press, pp. 273–285.
Zhang, J., Yan, S., Yuan, D., Alici, G., Nguyen, N.-T., Warkiani, M.E., Li, W., 2016. Fundamental and applications of inertial microfluidics: a review. Lab Chip 16, 10–34.